



**HAL**  
open science

## **Astroglial-Kir4.1 in Lateral Habenula Drives Neuronal Bursts to Mediate Depression**

Yihui Cui, Yan Yang, Zheyi Ni, Yiyan Dong, Guohong Cai, Alexandre Foncelle, Shuangshuang Ma, Kangning Sang, Siyang Tang, Yuezhou Li, et al.

► **To cite this version:**

Yihui Cui, Yan Yang, Zheyi Ni, Yiyan Dong, Guohong Cai, et al.. Astroglial-Kir4.1 in Lateral Habenula Drives Neuronal Bursts to Mediate Depression. *Nature*, 2018, 554, pp.323-327. 10.1038/nature25752 . hal-01683191

**HAL Id: hal-01683191**

**<https://hal.science/hal-01683191v1>**

Submitted on 12 Jan 2018

**HAL** is a multi-disciplinary open access archive for the deposit and dissemination of scientific research documents, whether they are published or not. The documents may come from teaching and research institutions in France or abroad, or from public or private research centers.

L'archive ouverte pluridisciplinaire **HAL**, est destinée au dépôt et à la diffusion de documents scientifiques de niveau recherche, publiés ou non, émanant des établissements d'enseignement et de recherche français ou étrangers, des laboratoires publics ou privés.

1 **Astroglial-Kir4.1 in Lateral Habenula Drives Neuronal Bursts to**  
2 **Mediate Depression**

3  
4 Yihui Cui<sup>1</sup>, Yan Yang<sup>1</sup>, Zheyi Ni<sup>1</sup>, Yiyan Dong<sup>1</sup>, Guohong Cai<sup>3</sup>, Alexandre Foncelle<sup>4</sup>,  
5 Shuangshuang Ma<sup>1</sup>, Kangning Sang<sup>1</sup>, Siyang Tang<sup>1</sup>, Yuezhou Li<sup>1</sup>, Ying Shen<sup>1</sup>, Hugues  
6 Berry<sup>4</sup>, Shengxi Wu<sup>3</sup>, Hailan Hu<sup>1,2\*</sup>  
7

8 <sup>1</sup>Center for Neuroscience, Key Laboratory of Medical Neurobiology of the Ministry of  
9 Health of China, School of Medicine, Interdisciplinary Institute of Neuroscience and  
10 Technology, Qiushi Academy for Advanced Studies, Zhejiang University, Hangzhou 310058,  
11 P.R. China

12 <sup>2</sup> Mental Health Center, School of Medicine, Zhejiang University, Hangzhou 310013, P.R.  
13 China

14 <sup>3</sup>Department of Neurobiology, Fourth Military Medical University, Xi'an, 710032, P.R.  
15 China

16 <sup>4</sup>INRIA, France; University of Lyon, France  
17  
18  
19  
20

21 \* Author for correspondence: [huhailan@zju.edu.cn](mailto:huhailan@zju.edu.cn)

22 Tel: +86-(0)571-8898-1720

23 Fax: +86-(0)571-8820-8920  
24  
25  
26  
27  
28

29 **Keywords: depression, lateral habenula, bursting, Kir4.1, inward-rectifying potassium**  
30 **channel, astrocyte, neuron-glia interaction, potassium buffering, firing mode**  
31

## Summary

32  
33  
34  
35  
36  
37  
38  
39  
40  
41  
42  
43  
44  
45  
46  
47

**Enhanced bursting activity of the lateral habenula (LHb) neurons is essential in driving depressive-like behaviors, but the cause of this increased bursts remained unknown. Here using high-throughput quantitative proteomic screen, we identified an astroglial potassium channel, Kir4.1, to be upregulated in the LHb of animal models of depression. Kir4.1 in the LHb shows a distinct expression pattern on the astrocytic membrane processes tightly wrapping around the neuronal soma. Electrophysiology and modeling data demonstrate that the level of Kir4.1 on astrocytes tightly regulates the degree of membrane hyperpolarization and the amount of burst activity of LHb neurons. Astrocyte-specific gain and loss of Kir4.1 functions in the LHb bidirectionally regulate neuronal bursting and depressive-like symptoms. Together, these results reveal a new form of glial-neural interaction in setting neuronal firing mode in a devastating psychiatric disease, and discover the therapeutic potential of targeting LHb Kir4.1 for treating major depression.**

48 A major breakthrough in neuroscience has been the discovery that astrocytes intimately interact  
49 with neurons to support and regulate a series of essential functions to foster brain information  
50 processing<sup>1-7</sup>. A wealth of investigations has focused on the astroglial-neural interactions at the  
51 tripartite synapses, where astrocyte processes tightly wrap around pre- and post-synaptic sites<sup>8</sup>.  
52 In contrast, not as much attention has been placed on astroglial-neural interaction in proximity to  
53 neuronal soma<sup>9,10</sup>. Particularly, how astrocytes regulate intrinsic firing patterns of neurons, and  
54 what structural basis may underlie this regulation, are much less explored.

55

56 Despite the surging interest of lateral habenula (LHb) in negative emotion<sup>11-20</sup>, only limited  
57 attention has been given to astrocytes and their potential roles in LHb hyperfunction in  
58 depression<sup>21</sup>. In the accompanying paper, we demonstrate that bursting activity of LHb  
59 neurons are greatly enhanced in animal models of depression. LHb burst drives depressive-  
60 like behaviors and is a prominent target of the rapid antidepressant ketamine. However, the  
61 cause of this enhanced burst of LHb neurons remains unsolved.

62

## 63 **Results**

### 64 **Kir4.1 is upregulated in LHb of animal models of depression**

65 In an unbiased, high-throughput, quantitative proteomic screening to compare habenular  
66 protein expression of congenitally learned helpless (cLH) rats<sup>22</sup> and wild-type SD rats, we  
67 identified Kir4.1 to be highly upregulated in the LHb of cLH rats<sup>11</sup> (1.69-fold of wild-type  
68 control,  $p = 0.02$ , Student's *t*-test, Fig. 1a). Western blot analysis confirmed that Kir4.1 had a  
69 significant increase (1.44-fold,  $p = 0.009$ , Paired *t*-test) in the membrane protein extraction of  
70 cLH habenulae (Fig. 1b). In contrast, another astrocyte-specific protein, glial fibrillary acidic  
71 protein (GFAP), did not show any change in expression (Extended Data Fig. 1a), indicating  
72 there was no astrogliosis.

73

74 To test whether Kir4.1 upregulation is universal in depression, we examined an additional rat  
75 model of depression, the LPS (lipopolysaccharide)-induced depression<sup>23</sup>. One week of LPS  
76 injection (0.5mg/kg, i.p.) in 3-month-old Wistar rats was sufficient to cause strong  
77 depressive-like phenotype in the forced swim test (FST, Extended Data Fig. 2e)<sup>23</sup> and sucrose  
78 preference test (SPT)<sup>23</sup>. The Kir4.1 level was also significantly increased in the LPS-induced  
79 rats (1.87-fold,  $p < 0.0001$ , Paired  $t$ -test, Fig. 1c). Quantitative real-time PCR revealed an  
80 increase (1.2-fold,  $p = 0.015$ , Paired  $t$ -test) of Kir4.1 mRNA level in cLH habenulae (Fig. 1d),  
81 suggesting that at least part of the protein level change is due to transcriptional upregulation.

82

### 83 **Age-dependent increase of LHb astrocytic Kir4.1 current and depression onset in cLH** 84 **rats**

85 Kir4.1 is a principal component of the glial Kir channel and is largely responsible for  
86 mediating the K<sup>+</sup> conductance and setting the resting membrane potential (RMP) of  
87 astrocytes<sup>24</sup>. To confirm that Kir4.1 function is indeed upregulated, we performed whole-cell  
88 patch clamp onto the astrocytes in brain slices made from the LHb of cLH or SD rats.  
89 Astrocytes were distinguished from neurons by their small (5–10  $\mu\text{m}$ ) oval shaped somata  
90 and electrophysiological features including a relatively hyperpolarized RMP ( $-74 \pm 1$  mV), a  
91 low input resistance  $R_{in}$  ( $47 \pm 6$  M $\Omega$ ), a linear I–V relationship and an absence of action  
92 potentials in response to depolarizing current injections (Extended Data Fig. 2a-d)<sup>25-27</sup>.  
93 Biocytin filling and absence of NeuN co-staining confirmed that cells fitting the above  
94 criteria were indeed astrocytes (Extended Data Fig.3). We then bath applied Ba<sup>2+</sup> (BaCl<sub>2</sub>, 100  
95  $\mu\text{M}$ ), which selectively blocks Kir channels at sub-mM concentrations, to isolate Kir4.1  
96 current<sup>25</sup> (Extended Data Fig. 2a, c). The Ba<sup>2+</sup>-sensitive current displayed a reversal potential  
97 close to  $E_k$  ( $-90\text{mV}$ )<sup>25,28</sup> (Fig. 1e, f), indicating that it represents the K<sup>+</sup> conductance. We

98 found that Ba<sup>2+</sup>-sensitive currents in LHb astrocytes were almost doubled in cLH rats (Fig.  
99 1e), as well as in LPS-treated rats (Extended Data Fig. 2f), at the age of P60-90.

100

101 Interestingly, the increase of Kir4.1 current and protein level was not obvious at P30 (Fig. 1f,  
102 Extended data Fig. 1b). At this age, cLH rats did not yet show depressive-like phenotypes in  
103 both the FST (Fig. 1g) and learned helpless test (LHT, Fig. 1h), suggesting that the  
104 upregulation of Kir4.1 level is concomitant with the developmental onset of the depressive-  
105 like symptoms.

106

### 107 **Kir4.1 are expressed on astrocytic processes tightly wrapping around neuronal soma**

108 As an inwardly rectifying K<sup>+</sup> channel, Kir4.1 has been strongly implicated in buffering  
109 excess extracellular K<sup>+</sup> in tripartite synapses<sup>24,29-31</sup>. Conventional model of K<sup>+</sup> buffering  
110 suggests Kir4.1 to be highly expressed in astrocytic endfeet surrounding synapses<sup>32-34</sup>.  
111 Surprisingly, with immunohistochemistry co-labeling, Kir4.1 staining in LHb appeared to  
112 overlap with the neuronal marker NeuN at low magnification (20X, Extended Data Fig. 4a),  
113 although in the same brain slice Kir4.1 staining patterns in hippocampus were typical  
114 astrocytic-looking (Extended Data Fig. 4b). However, higher magnification imaging with  
115 single layer scanning (0.76μm per layer) revealed that Kir4.1 staining enveloped NeuN  
116 signals (Fig. 2a). To confirm that Kir4.1 indeed locates within astrocytes but not neurons in  
117 LHb, we separately knocked it out in either neurons or astrocytes by injecting AAV virus  
118 expressing the cre recombinase under either the neuronal promoter CaMKII or glial promoter  
119 GFAP (gfaABC1D)<sup>26,35</sup> into Kir4.1<sup>f/f</sup> floxed mice<sup>25</sup>. The staining of Kir4.1 remained intact  
120 with neuronal knock-out, but was completely eliminated with astrocytic knock-out (Fig. 2b).  
121 Electron microscopy imaging revealed that Kir4.1-positive gold particles were distributed  
122 encircling the membrane of neuronal cell bodies (Fig. 2c, Extended Data Fig. 5a, b), as well

123 as in the synapses (Extended Data Fig. 5d). Consistently, whole-cell-patch recordings showed  
124 that Ba<sup>2+</sup>-sensitive currents were absent in neurons but abundant in astrocytes in the LHb (Fig.  
125 2d, Extended Data Fig. 6). Together these results suggest that Kir4.1 is mainly expressed in  
126 astrocytic processes tightly wrapping around neuronal soma and synapses in the LHb.

127

### 128 **Overexpression of kir4.1 in LHb astrocytes increases neuronal bursts and causes strong** 129 **depressive-like behaviors**

130 To test the consequence of Kir4.1 upregulation in LHb, we used adeno-associated viruses of  
131 the 2/5 serotype (AAV2/5) that preferentially target astrocytes<sup>26</sup> together with the human  
132 GFAP (gfaABC1D) promoter<sup>26,35</sup> to deliver GFP-tagged Kir4.1 channels (AAV-  
133 GFAP::Kir4.1) or AAV-GFAP::GFP as a control (Fig. 3a). 14 days after bilateral injection in  
134 the LHb at P50, AAV2/5-mediated viral transfection led to Kir4.1 and GFP expression in  
135 astrocytes throughout the LHb (Fig. 3b). The specificity of the viral infection in astrocytes  
136 was verified by co-immunostaining of NeuN and GFP: only 0.3% NeuN+ cells (n = 2668)  
137 were infected by this virus (Extended Data Fig.7). We made whole-cell recordings from  
138 either astrocytes or neurons surrounding the viral-transfected astrocytes in coronal LHb slices  
139 (Fig. 3c-e). The RMPs of both astrocytes and neurons were more hyperpolarized (Fig. 3d, e)  
140 and the percentage of bursting neurons were significantly higher (Fig.3f) in mice infected  
141 with AAV-GFAP::Kir4.1 than with AAV-GFAP::GFP.

142

143 We then assayed depressive-like phenotypes and found that mice with AAV-GFAP::Kir4.1  
144 infection in the LHb displayed severe depressive-like behaviors, including increased  
145 immobile duration (p = 0.0002, Unpaired *t*-test) and decreased latency to immobility (p =  
146 0.001, Unpaired *t*-test) in FST (Fig. 3g), and decreased sucrose preference in the SPT (p <

147 0.0001, Unpaired *t*-test, Fig. 3h), while the general locomotion was unchanged (Extended  
148 Data Fig. 8a-b).

149

### 150 **Kir4.1-mediated K buffering regulates neuronal RMP and bursting activity**

151 How does an astrocytic potassium channel regulate RMP and burst firing of the LHb neuron?

152 We hypothesize that within the highly confined extracellular space between neuronal soma

153 and Kir4.1-positive astrocytic processes (Fig. 2), the constantly-released K<sup>+</sup> from

154 intrinsically active LHb neurons is quickly cleared by astrocytes through a Kir4.1-dependent

155 mechanism. Accordingly, we predict that blockade of Kir4.1 should compromise K<sup>+</sup> spatial

156 buffering, resulting in increased extracellular K<sup>+</sup> (K<sub>out</sub>), and according to Nernst Equation,

157 depolarized neuronal RMPs (modeled in Extended Data Fig. 9). Consistent with this

158 prediction, blocking Kir4.1 with BaCl<sub>2</sub> depolarized the RMPs of LHb neurons, after about 10

159 min bath perfusion of BaCl<sub>2</sub> (Fig. 4a). The amount of changes in RMP positively correlated

160 with the original firing rates of neurons (Fig. 4b), indicating that the more active the neuron is,

161 the larger contribution the K<sup>+</sup> buffering to its RMP. Similar amount of RMP change was

162 induced when BaCl<sub>2</sub> was applied in presence of synaptic transmission blockers (picrotoxin,

163 NBQX and AP5, Extended Data Fig. 10), suggesting that Kir4.1-dependent regulation of

164 LHb neuronal RMP occurs mostly at neuronal cell bodies instead of at synaptic sites.

165 Consequent to the RMP change, perfusion of BaCl<sub>2</sub> caused a dramatic increase of firing

166 frequency until the neuron reached a sustained plateau of a tetanus response and stopped

167 firing (Fig. 4c).

168

169 Vice versa, upregulation of Kir4.1 or stop neuronal firing should decrease extracellular K<sup>+</sup>

170 (K<sub>out</sub>) and hyperpolarize neuronal RMPs. Indeed, overexpression of Kir4.1 in astrocytes (Fig.

171 3e) or blocking neuronal APs by TTX (Fig. 4d, e) both caused hyperpolarization of LHb



172 neurons. Overexpression of Kir4.1 in astrocytes also increased neuronal bursts (Fig. 3g).  
173 Finally, to assess a causal relationship between  $K_{out}$  and firing mode, we made current-  
174 clamp recordings of LHb neurons while lowering  $K_{out}$  from 2.75mM to 1.4mM (Fig. 4f).  
175 This led to lowered neuronal RMP by 13.7 +/- 0.5mV and a direct shift of originally tonic-  
176 firing neurons (8 out of 15) into bursting mode (Fig. 4g). Consequently, percentage of  
177 bursting neurons was increased from 8% to 23% ( $p < 0.0001$ , Chi-square test, Fig. 4h). In  
178 summary, by increasing astrocytic Kir4.1 expression or decreasing the extracellular  $K^+$   
179 concentration, we were able to phenocopy in WT animals several key neuronal properties  
180 observed in the LHb of animal models of depression, namely hyperpolarized RMPs and  
181 enhanced bursts. These results indicate that enhanced capacity of extracellular K clearance  
182 due to Kir4.1 overexpression may underlie the neuronal hyperpolarization required for burst  
183 initiation.

184

### 185 **Loss-of-function of Kir4.1 in LHb decreases neuronal bursting and rescues depressive-** 186 **like phenotypes**

187 Next, to determine whether loss-of-function of Kir4.1 in the LHb may reduce neuronal bursts  
188 and reverse depressive phenotypes, we devised two strategies, by using AAV2/5 viral vectors  
189 to express either a short hairpin RNA (shRNA) to knock down the level of Kir4.1, or a  
190 dominant negative construct to block its function in the LHb of cLH rats (Fig. 5a). We tested  
191 six shRNAs specifically targeting the Kir4.1 transcript in cell culture and chose the one with  
192 most efficient knock-down efficiency (Fig. 5b and Extended Data Fig. 11a) for viral package.  
193 To avoid an off-target effect of shRNA, we also used a dominant-negative form of Kir4.1,  
194 dnKir4.1, containing a GYG to AAA point mutation at the channel pore, which blocks  $K^+$   
195 channels<sup>36</sup> (Extended Data Fig. 11b, 12, Fig. 5c). We first examined the effect of Kir4.1-  
196 shRNA on glial and neural electrophysiological properties. In astrocytes infected with the

197 AAV-H1::Kir4.1-shRNA, we observed a dramatic change of I-V relation (Fig. 5d), a 32 mV  
198 depolarization compared with non-infected astrocytes ( $p < 0.0001$ , One-way ANOVA) and  
199 41mV depolarization compared with ctrl-shRNA-infected astrocytes ( $p < 0.0001$ , One-way  
200 ANOVA, Fig. 5e), consistent with the literature that Kir4.1 is majorly responsible for setting  
201 the astrocytic RMPs<sup>25</sup>. In neurons infected with the AAV-H1::Kir4.1-shRNA, the RMPs did  
202 not differ from neighboring non-infected neurons (because neurons do not express Kir4.1  
203 endogenously, Fig. 5f). However, RMPs of neighboring LHb neurons from AAV-H1::Kir4.1-  
204 shRNA-infected brain slices were overall more depolarized than RMPs of those from AAV-  
205 H1::Ctrl-shRNA-infected rats ( $-43 \pm 2\text{mV}$  vs.  $-53 \pm 2.7\text{mV}$ ,  $p = 0.006$ , One-way ANOVA,  
206 Fig. 5f), suggesting that knock-down of Kir4.1 in astrocytes had a global impact on RMPs of  
207 neighboring neurons. Similar effects were observed in AAV-GFAP::dnKir4.1 infected LHb  
208 slices (Extended Data Fig. 11c-f). Most importantly, bursting activity in the LHb of cLH rats  
209 were significantly eliminated by AAV-H1::Kir4.1-shRNA (Fig. 5g) and AAV-  
210 GFAP::dnKir4.1 (Extended Data Fig. 11f) infection.

211

212 Behaviorally, infection of AAV-H1::Kir4.1-shRNA or AAV-GFAP::dnKir4.1 had a  
213 pronounced effect on rescuing the depressive-like phenotypes of cLH rats in three depression  
214 paradigms: reducing the immobility time ( $p = 0.01$ , Unpaired  $t$ -test, Fig. 5h) and increasing  
215 latency to immobility ( $p = 0.0018$ , Unpaired  $t$ -test, Fig. 5h) in FST, increasing bar pressing  
216 number in the LHT ( $p = 0.0004$ , Unpaired  $t$ -test, Fig. 5i, j), and increasing the sucrose  
217 preference score in SPT ( $p = 0.04$ , Unpaired  $t$ -test, Fig. 5k). The behavior scores in LHT  
218 clearly correlated with those in FST (Fig. 5l).

219

220 Here we discover an important function of Kir4.1 at the highly specialized neuron-glia  
221 interface in the LHb in regulating neuronal RMP and firing pattern. During depression, the

222 upregulation of Kir4.1 may cause enhanced capacity of extracellular K clearance, leading to a  
223 decrease of K<sub>out</sub> and neuronal hyperpolarization (Fig. 5m). As demonstrated in our  
224 accompanying manuscript, neuronal hyperpolarization may de-inactivate T-type voltage-  
225 sensitive calcium channels (T-VSCCs) which in turn initiate NMDAR-dependent bursts to  
226 cause a stronger suppression of the downstream monoaminergic centers (Fig. 5m). These  
227 results may inspire the development of novel treatments of major depression targeting on  
228 maladaptive neuron-glia interactions in the LHb.

229

230

### 231 **Acknowledgements**

232

233 We thank Dr. Ken McCarthy for gift of Kir4.1<sup>fl/fl</sup> floxed mice; Baljit Khakh for GFAP-Kir4.1  
234 plasmid; Jianhong Luo for HEK293 cells; Guangping Gao for AAV-GFAP::GFP; Tian Xue  
235 for advice on dn-Kir4.1 design; Yingying Liu for technical support on electromicroscopy  
236 experiment; Chenjie Shen for help with immunohistochemistry; Yudong Zhou, Shumin Duan,  
237 Jingwei Zhao and Xiaohui Zhang for advices on experimental design; Christian Giaum and  
238 Pierre Magistretti for comments on manuscript. Patent applied for 201710322245.X. This  
239 work was supported by grants from the Ministry of Science and Technology of China  
240 (2016YFA0501000), the National Natural Science Foundation of China (91432108,  
241 31225010, and 81527901), the Strategic Priority Research Program (B) of the Chinese  
242 Academy of Sciences (XDB02030004), 111 project (B13026) to H. H.

243

### 244 **Author contributions**

245 H.H. and Y.C. designed the study. Y.C. performed the *in vitro* patch recordings; Y.Y.  
246 performed the biochemistry and immunohistochemistry experiments; Y.C., Y.Y., Y.D. and  
247 K.S. performed viral injections and behavioral experiments; Z.N., A.F. and H.B. established

248 the biophysical model; S.M. assisted cell culture experiments; G.C. and S.W. conducted the  
249 EM experiments; Y.S. contributed Kir4.1<sup>ff</sup> floxed mice; S.T. and Y.L. constructed plasmids.  
250 H.H. wrote the manuscript with the assistance of Y.C., Y.Y. and Z.N..

251

252 **Methods**

253

254 **Animals.** Male cLH rats (3-4 weeks or 8-12 weeks of age) and age-matched male Sprague  
255 Dawley rats (SLAC Laboratory Animal Co., Shanghai) were used. The cLH rats were  
256 screened by learned helpless test<sup>1,2</sup> for breeding as previously described<sup>1</sup>. Male Wistar rats  
257 (SLAC Laboratory Animal Co., Shanghai, 12 weeks) were used for establishing the LPS-  
258 induced depressive-like rat model. Male adult (7-8 weeks of age) C57BL/6 mice (SLAC) or  
259 Kir4.1<sup>ff</sup> floxed mice (originally obtained from Dr. Ken McCarthy at University of North  
260 Carolina) were used for virus injection the immunohistochemistry experiments. Animals  
261 were group-housed two/cage for rats and four/cage for mice under a 12-h light-dark cycle  
262 (light on from 7 a.m. to 7 p.m.) with free access to food and water *ad libitum*. All animal  
263 studies and experimental procedures were approved by the Animal Care and Use Committee  
264 of the animal facility at Zhejiang University.

265

266 **Western Blot.** The habenular membrane fraction and whole protein was extracted as  
267 previously described<sup>11</sup>. Animals were anesthetized using 10% chloral hydrate, and habenular  
268 tissue was quickly dissected from the brain and homogenized in lysis buffer (320 mM  
269 sucrose, 4 mM HEPES pH7.4, 1 mM MgCl<sub>2</sub> and 0.5 mM CaCl<sub>2</sub>, 5 mM NaF, 1 mM Na<sub>3</sub>VO<sub>4</sub>,  
270 EDTA-free, Protease Inhibitor cocktail tablets (Roche) on ice. The lysis buffer used for  
271 extracting the total protein of HEK293TN cell contained 50mM Tris (pH 7.4), 150mM NaCl,  
272 1% Triton X-100, 1% sodium deoxycholate, 0.1% SDS and Protease Inhibitor cocktail tablets  
273 (Roche). After protein concentration measurement by BCA assay, 10~20μg proteins for each  
274 lane was separated on a 10% SDS-PAGE gel and transferred for western blot analysis. Anti-  
275 Kir4.1 (1:1000, Alomone labs), anti-GFAP (1:1000, Sigma) and anti-tubulin (1:5000, Bio-  
276 Rad) antibodies, and high sensitive ECL reagent (GE Healthcare) were used. All the bands  
277 were analyzed with Quantity one or Image J.

278 **Immunohistochemistry.** Animals were anesthetized using 10% chloral hydrate, and then  
279 perfused transcardially with ice-cold PBS (pH 7.4) followed by 4% paraformaldehyde. After  
280 overnight post fix in 4% paraformaldehyde solution, brains were cryoprotected in 30%  
281 sucrose for 1 day (for mice) or 3 days (for rats). Coronal sections (40  $\mu$ m) were cut on a  
282 microtome (Leica) and collected in PBS and stored at 4°C for further using. The antibodies  
283 used were rabbit anti-Kir4.1 extracellular peptide (1:200, Alomone labs), mouse anti-GFAP  
284 (1:500, Sigma), mouse anti-NeuN (1:500, Millipore), Rabbit anti NeuN (1:500, Millipore),  
285 mouse anti-S100b (1:500, Sigma), chicken anti-GFP (1:1000, Abcam), Mouse anti-Flag  
286 (1:1000, Beyotime), Alexa Fluor 488 goat anti-rabbit IgG, Alexa Fluor 488 goat anti-chicken  
287 IgG, Alexa Fluor 546 goat anti-mouse IgG (all 1:1000, Invitrogen). Specifically, for Kir4.1  
288 staining, the rabbit anti-Kir4.1 extracellular peptide antibody was incubated for 48-72 h and  
289 the other primary antibodies were incubated for 36-48 h. For the antibody absorption  
290 experiments, the rabbit anti-Kir4.1 extracellular peptide antibody was pre-adsorbed with the  
291 Kir4.1 antigen by mixing at the weight ratio of 1:2 for 24 h. Slices were counterstained with  
292 Hoechst in the final incubation step to check the injection site. Fluorescent image acquisition  
293 was performed with an Olympus Fluoview FV1000 confocal microscope and a Nikon A1  
294 confocal microscope.

295

296 **Cell transfection and cell culture.** HEK293 cells (gift from Jianhong Luo) were used for the  
297 electrophysiology recording and HEK293TN cells (Taitool Bioscience, China) were used for  
298 western blot analysis. Cells used in this study were authenticated and checked for  
299 mycoplasma contamination. The plasmids used were pAAV-Ubi-Kir4.1-2A-eGFP, pAAV-  
300 Ubi-dnKir4.1 (GYG to AAA)-2A-eGFP, pAAV-CAG-eGFP, pAAV-H1-Kir4.1-shRNA-  
301 CAG-eGFP and pAAV-H1-Luciferase-shRNA-CAG-eGFP. HEK293 cells were trypsinized  
302 for 5 min using 0.25% trypsin (wt/vol), and replated onto glass coverslips in fresh

303 DMEM:F12 medium (Life Technologies) containing 1 mM nonessential amino acids (Gibco),  
304 1 mM sodium pyruvate (Gibco), and 10% FBS (Hyclone). Cells were transfected using  
305 Lipofectamine 2000 (Invitrogen) according to standard protocols, then cultured for 5-6 h in  
306 well plates at 37 °C in a humid atmosphere of 5% CO<sub>2</sub> and 95% air. Cells were cultured for  
307 another 48 h before western blot or electrophysiology experiments.

308

309 **Plasmid constructs.** The pAAV-Ubi-Kir4.1-2A-eGFP plasmid was assembled by  
310 homologous recombination of AAV backbone linearized from the AAV-Ubi-CaMKII-2A-  
311 eGFP plasmid<sup>11</sup> by PCR and Kir4.1 amplified from pZac2.1- gfaABC1D-EGFP-Kir4.1  
312 plasmid (AddGene). The pAAV-Ubi-dnKir4.1 (GYG to AAA)-2A-eGFP plasmid was made  
313 by PCR-based mutagenesis using pAAV-Ubi-Kir4.1-2A-eGFP as a backbone (Fw: 5'-  
314 AAAGATGGCCGGAGCAACGTGAGAATGGAGCATATTGCT-3'; Rev: 5'-  
315 GCTGATGTAGCGGAAGGCGGCGGCAATGGTGGTCTGGGATTCGAGGGA-3'). The  
316 pAAV-gfaABC1D- dnKir4.1 (GYG to AAA)-2A-EGFP was assembled by homologous  
317 recombination of pZac2.1 gfaABC1D backbone linearized from the pZac2.1- gfaABC1D-  
318 EGFP-Kir4.1 plasmid (AddGene) by PCR and Kir4.1dn-2A-EGFP sequence amplified from  
319 pAAV-Ubi-dnKir4.1 (GYG to AAA)-2A-eGFP plasmid. The pAAV-H1-Kir4.1-shRNA-  
320 CAG-eGFP was constructed using a vector (provide by Taitool Bioscience, China), which  
321 contains a CAG promoter driving eGFP and a H1 promoter driving shRNA expression. We  
322 designed 6 shRNA sequences by RNAi designer online software (Invitrogen) as indicated  
323 below:

324 1) 5'-GGACGACCTTCATTGACAT-3';

325 2) 5'-GCTACAAGCTTCTGCTCTTCT-3';

326 3) 5'-GCTCTTCTCGCCAACCTTTAC-3';

327 4) 5'-CCGGAACCTTCCTTGCAAA-3';

328 5) 5'-GCGTAAGAGTCTCCTCATTGG-3'

329 6) 5'-GCCCTTAGTGTGCGCATTA-3'.

330 We then tested the knock-down efficiency by Western blot of Kir4.1 from HEK293TN cells  
331 which were co-transfected with Flag-tagged-Kir4.1 plasmid (pAAV-CMV-betaGlobin-  
332 Kir4.1-eGFP-3Flag) and each of the six shRNA plasmids. Based on our western blot result  
333 (Extended Figure 11a), we chose the fifth sequence, 5'-GCGTAAGAGTCTCCTCATTGG-  
334 3', for Kir4.1-shRNA virus package.

335

336 **Electron microscopic immunohistochemistry.** Four mice were deeply anesthetized with  
337 1% sodium pentobarbital intraperitoneally (50 mg/kg body weight) and perfused  
338 transcardially with 20ml saline, followed by 40ml ice-cold mixture of 4% paraformaldehyde  
339 and 0.05% glutaraldehyde in 0.1M PB for 1 h. Brainstems were removed and postfixed by  
340 immersion in the same fixative for 4 h at 4°C. Serial coronal sections of 50 µm thickness  
341 were prepared with a vibratome (VT 1000S, Leica), and approximately 18-20 sections,  
342 including the LHb region, were collected from each brain.

343

344 Kir4.1 was detected by the immunogold-silver staining. Briefly, sections were blocked with  
345 blocking buffer (5% BSA, 5% NGS and 0.05% Triton X-100 in PBS), and then incubated  
346 overnight in the primary antibodies of rabbit anti-Kir4.1 (1:200) diluted with solution  
347 containing 1% BSA, 1% NGS and 0.05% Triton X-100. The secondary antibody was anti-  
348 rabbit IgG conjugated to 1.4 nm gold particles (1:100, Nanoprobes, Stony Brook, NY) for 4 h.  
349 After rinsing, sections were post fixed in 2% glutaraldehyde in PBS for 45 min. Silver  
350 enhancement was performed in the dark with HQ Silver Kit (Nanoprobes) for visualization of  
351 Kir4.1 immunoreactivity. Before and after the silver enhancement step, sections were rinsed  
352 several times with de-ionized water.



353

354 Immuno-labeled sections were fixed with 0.5% osmium tetroxide in 0.1 M PB for 1 h,  
355 dehydrated in graded ethanol series, then in propylene oxide, and finally flat-embedded in  
356 Epon 812 between sheets of plastic. After polymerization, acrylic sheets were then peeled  
357 from the polymerized resin, and flat-embedded sections were examined under the light  
358 microscope. Three to four sections containing Kir4.1 immunoreactivity in the LHb were  
359 selected from each section, trimmed under a stereomicroscope, and glued onto blank resin  
360 stubs. Serial ultrathin sections were cut with an Ultramicrotome (Leica EM UC6, Germany)  
361 using a diamond knife (Diatome, PA) and mounted on formvar-coated mesh grids (6-8  
362 sections/grid). They were then counterstained with uranyl acetate and lead citrate, and  
363 observed under a JEM-1230 electron microscope (JEOL LTD, Japan) equipped with CCD  
364 camera and its application software (832 SC1000, Gatan, PA).

365

366 **Stereotaxic surgery and virus injection.** cLH rats (postnatal 50-60 days) were deeply  
367 anesthetized by using 4% pentobarbital. Mice (postnatal 50-60 days) were deeply  
368 anesthetized by ketamine (100 mg/kg of body weight) and xylazine (8 mg/kg). Animals were  
369 placed on a stereotactic frame (RWD Instruments, China). A small volume of virus was  
370 injected into bilateral LHb (for rats LHb: AP, -3.7 mm from bregma; ML,  $\pm$ 0.7 mm; DV, -  
371 4.55 mm from the brain surface; for mice: AP, -1.72 mm from bregma; ML,  $\pm$ 0.46 mm; DV,  
372 -2.62 mm from the brain surface) using a pulled glass capillary with a pressure microinjector  
373 (Picospritzer III, Parker, USA) at a slow rate of 0.1  $\mu$ l/min. After the injection was completed,  
374 the capillary was left for an additional 10 minutes before it was then slowly withdrawn  
375 completely. After surgery, animals were recovered from anesthesia under a heat pad.

376

377 AAV-CaMKII:EGFP-Cre (AAV2/1-CamKII-HI-EGFP-Cre, 0.2  $\mu$ l, bilateral into LHb,  
378 University of Pennsylvania vector core, Pennsylvania, USA), AAV2/5-GFAP::EGFP-Cre  
379 (AAV2/5-gfaABC1D-EGFP-Cre, titer:  $4.74 \times 10^{12}$  v.g./ml, dilution: 1:2, 0.2  $\mu$ l, bilateral into  
380 LHb, Taitool Bioscience, China), AAV-GFAP::Kir4.1 (AAV2/5-gfaABC1D-EGFP-Kir4.1,  
381 titer:  $9.19 \times 10^{12}$  v.g./ml, dilution: 1:5, 0.2  $\mu$ l, bilateral into LHb, Taitool Bioscience, China),  
382 AAV-GFAP::GFP (AAV2/5-gfaABC1D-EGFP, titer:  $1.61 \times 10^{13}$  v.g./ml, dilution: 1:5, 0.2  $\mu$ l,  
383 bilateral into LHb, University of Massachusetts, Guangping Gao Lab, USA), AAV-  
384 H1::Kir4.1-shRNA (AAV2/5-H1-Kir4.1-shRNA-CAG-EGFP, titer:  $3.04 \times 10^{13}$  v.g./ml,  
385 dilution: 1:10, 0.2  $\mu$ l, bilateral into LHb, Taitool Bioscience, China), AAV-H1::Ctrl-shRNA  
386 (AAV2/5-H1-Luciferase-shRNA-CAG-EGFP, titer:  $1.46 \times 10^{13}$  v.g./ml, dilution: 1:5, 0.2  $\mu$ l,  
387 bilateral into LHb, Taitool Bioscience, China), AAV2/5-gfaABC1D-dnKir4.1-2A-EGFP  
388 (GYG to AAA) (titer:  $4.15 \times 10^{13}$  v.g./ml, 0.2  $\mu$ l, bilateral into LHb, Taitool Bioscience,  
389 China). All viral vectors were aliquot and stored at -80 °C until use.

390

### 391 **Depression model and Behavior assay**

392 **LPS-induced depression.** The LPS-induced depression model was conducted as previously  
393 described<sup>22</sup>. Wistar male rats (3 months) were used for the experiments. LPS (Sigma, L-  
394 2880) dissolved in sterile 0.9% saline was intraperitoneally injected into Wistar rats, at a  
395 dosage of 0.5 mg/kg. This dosage was used to stimulate a subclinical infection without  
396 inducing obvious inflammation and other apparent impairments in animals. Saline or LPS  
397 was injected between 09:30 and 10:30 a.m. daily for 7 days. The forced swim test was  
398 performed 24 hours after the last injection. The habenular tissue was dissected 24 hours after  
399 the behavioral test and eletrophysiology experiments.

400

401 **Learned helpless test (LHT).** Male juvenile (P30) or adult (P90) cLH rats were tested in a  
402 lever-pressing task to evaluate the learned helpless (LH) phenotype<sup>11</sup>. A cue-light-illuminated  
403 lever in the shock chamber was presented, which can terminate the shock when rats pressed  
404 the lever. 15 escapable shocks (0.8 mA) were delivered with a 24 s inter-shock interval. Each  
405 shock lasted up to 60 s unless the rat pressed the lever to terminate the shock. Out of the 15  
406 trials, rats which failed to press the lever for more than 10 trials were defined as “learned  
407 helplessness” (LH), and rats with less than 5 failures were defined as “non-learned  
408 helplessness” (NLH).

409

410 **Forced swim test (FST).** Animals were individually placed in a cylinder (12 cm diameter, 25  
411 cm height for mice; 20 cm diameter, 50 cm height for rats) of water (23-25 °C) and swam for  
412 6 min under normal light<sup>3</sup>. Water depth was set to prevent animals from touching the bottom  
413 by tails and hind limbs. Animal behaviors were videotaped from the side. The immobility  
414 time during the last 4 min test was counted offline by an observer blind of the animal  
415 treatments. Immobility was defined as time when animals remained floating or motionless  
416 with only movements necessary for keeping balance in the water. For rats, an additional pre-  
417 test was conducted 24 h before the test, during which rats were individually placed in a  
418 cylinder of water with conditions described above for 15 min.

419

420 **Sucrose preference test (SPT).** Animals were single housed and habituated with two bottles  
421 of water for 2 days, followed by two bottles of 2% sucrose for 2 days<sup>3</sup>. Animals were then  
422 water deprived for 24 h and then exposed to one bottle of 2% sucrose and one bottle of water  
423 for 2 h in the dark phase. Bottle positions were switched after 1 h. Total consumption of each  
424 fluid was measured and sucrose preference was defined as the ratio of sucrose consumption  
425 divided by total consumptions of water and sucrose.

426 **Open field test (OFT).** Animals were placed in the center of an arena (40 cm x 40 cm x 40.5  
427 cm for mice; and 100 cm x 100 cm x 40 cm for rats) in a room with dim light for 10 min. A  
428 video camera positioned directly above the arena was used to track the movement of each  
429 animal (Any-maze, Stoelting, US).

430

431 **LHb brain slice preparation.** Rats (P25-30 or P60-90) and mice (P90) were anesthetized  
432 with isoflurane and 10% chloral hydrate, and then perfused with 20 ml ice-cold ACSF  
433 (oxygenated with 95 % O<sub>2</sub> + 5% CO<sub>2</sub>) containing (mM): 125 NaCl, 2.5 KCl, 25 NaHCO<sub>3</sub>,  
434 1.25 NaH<sub>2</sub>PO<sub>4</sub>, 1 MgCl<sub>2</sub> and 25 Glucose, with 1 mM pyruvate added. The brain was removed  
435 as quickly as possible after decapitation and put into chilled and oxygenated ACSF. Coronal  
436 slices containing habenular (350µm- and 300µm- thickness for rats and mice, respectively)  
437 were sectioned in cold ACSF by a Leica 2000 vibratome and then transferred to ASCF at  
438 32°C for incubation and recovery for 1h and then transferred to room temperature. ACSF was  
439 continuously gassed with 95% O<sub>2</sub> and 5% CO<sub>2</sub>. Slices were allowed to recover for at least 1  
440 hour before recording.

441

442 ***In vitro* electrophysiological recording.** For LHb neuron recordings, currents were  
443 measured under whole-cell patch clamp using pipettes with a typical resistance of 5–6 MΩ  
444 filled with internal solution containing (mM) 105 K-Gluconate, 30 KCl, 4 Mg-ATP, 0.3 Na-  
445 GTP, 0.3 EGTA, 10 HEPES and 10 Na-phosphocreatine, with pH set to 7.35. For the  
446 biocytin filling, 5mg/ml biocytin was added in the internal solution. The external ACSF  
447 solution contained (in mM) 125 NaCl, 2.5 KCl, 25 NaHCO<sub>3</sub>, 1.25 NaH<sub>2</sub>PO<sub>4</sub>, 1 MgCl<sub>2</sub> and 25  
448 Glucose. Cells were visualized with infrared optics on an upright microscope (BX51WI,  
449 Olympus). A MultiClamp 700B amplifier and pCLAMP10 software were used for electro-  
450 physiology (Axon Instruments). The series resistance and capacitance was compensated

451 automatically after stable Giga seal were formed. The spontaneous neuronal activity was  
452 recorded under current-clamp ( $I = 0$  pA) for consecutive 60 s. RMP was determined during  
453 the silent period of the neuronal spontaneous activity.

454

455 To test TTX ( $1 \mu\text{M}$ , Sigma) and  $\text{BaCl}_2$  ( $100 \mu\text{M}$ , Sigma) effect onto neuronal RMP and  
456 spontaneous activity, baselines were recorded for at least for 3 min. Drug were then perfused,  
457 the arrival of the drug was precisely indicated with a bubble that was pre-added before the  
458 transition from normal ACSF to drug added ACSF. TTX effect on LHb neuronal RMP and  
459 spontaneous activity was stabilized after several minutes while  $\text{BaCl}_2$  effect on neuronal RMP  
460 and spontaneous activity took more than 10 min to stabilize. We thus analyzed the drug effect  
461 of TTX and  $\text{BaCl}_2$  at the time point of 5min and 15 min respectively.

462

463 **Astrocytic whole-cell patch clamp and Kir4.1 current isolation.** Astrocytes were  
464 distinguished from neurons by their small ( $5\text{-}10 \mu\text{m}$ ) oval-shaped somata and by distinct  
465 electrophysiological features: a hyperpolarized RMP and a low input resistance, a linear I-V  
466 relationship and an absence of action potentials in response to increased injection currents.  
467  $\text{BaCl}_2$  ( $100\mu\text{M}$ , Sigma) were applied to isolate Kir4.1 current which is subtracted from the IV  
468 curve recorded from  $-120\text{mV}$  to  $0\text{mV}$ . Biocytin (Sigma)  $5\text{mg/ml}$  was dissolved into the  
469 patch-clamp pipette solution. After electrophysiological characterization, cells are held for at  
470 least 30 minutes in voltage clamp and constantly injected with a hyperpolarization current  
471 ( $500$  ms,  $50$  pA,  $0.5$  Hz,  $30$  min) to allow biocytin filling (performed at  $34^\circ\text{C}$ ). Subsequently,  
472 slices were fixed overnight in  $4\%$  paraformaldehyde at  $4^\circ\text{C}$ . The antibodies used were rabbit  
473 anti-NeuN ( $1:500$ , Millipore), Alexa Fluor 546 donkey anti-rabbit IgG ( $1:1000$ , Invitrogen),  
474 Cy2-conjugated Streptavidin ( $1:1000$ , Jackson ImmunoResearch). Fluorescent image  
475 acquisition was performed with a Nikon A1 confocal microscope.

476 **Tri-compartment model.**

477 Tri-compartment model was constructed including the neuron, the astrocyte and the  
 478 extracellular space. The model is based on ionic fluxes between three compartments. Na<sup>+</sup> and  
 479 K<sup>+</sup> voltage-gated channel, and leak channel were recruited into the neuron as:

480 
$$dV_N/dt = (I_{app} - I_K - I_{Na} - I_{Leak,N})/c_N$$

481 where  $V_N$  is the neuronal membrane potential,  $c_N$  is the neuronal capacitance.  $I_{app}$  is the  
 482 external current applied to the neuron.  $I_{Na}$  and  $I_K$  are the fast Na<sup>+</sup> and K<sup>+</sup> currents responsible  
 483 for the generation of action potentials;  $I_{Leak,N}$  are responsible for the neuronal resting  
 484 membrane potential. Kir4.1 channel on the extracellular and vessel side and leak channel  
 485 were recruited into the astrocyte as:

486 
$$dV_A/dt = (-I_{Kir} - I_{Kir\_vess} - I_{Leak,A})/c_A$$

487 where  $V_A$  is the astrocytic membrane potential,  $c_A$  is the astrocytic capacitance.  $I_{Kir}$  are  
 488 outward during the resting state, while become inward when K<sup>+</sup> equilibrium potential  
 489 exceeds the astrocytic membrane potential.  $I_{Kir\_vess}$  accounts for the K<sup>+</sup> outflow from the  
 490 astrocyte from the vessel side.  $I_{Leak,A}$  are responsible for the astrocytic resting membrane  
 491 potential.

492 The equations of the K<sup>+</sup> in the three compartments are described by:

493 
$$d[K^+]_o/dt = (I_{kir} + I_k)/(F \cdot vol_o) - 2 \cdot (i_{pump,N} + i_{pump,A}) - d_{K_o} \cdot ([K^+]_o - K_{o_o})$$

494 
$$d[K^+]_N/dt = -I_k/(F \cdot vol_N) + 2 \cdot i_{pump,N} \cdot vol_o/vol_N - d_{K_N} \cdot ([K^+]_N - K_{N_o})$$

495 
$$d[K^+]_A/dt = (-I_{kir} - I_{kir\_vess})/(F \cdot vol_A) + 2 \cdot i_{pump,A} \cdot vol_o/vol_A - d_{K_A} \cdot ([K^+]_A - K_{A_o})$$

496 The extracellular K<sup>+</sup> is mainly contributed by  $I_K$ . Released extracellular K<sup>+</sup> from the neuron  
 497 is taken up by through Kir4.1 channels and Na<sup>+</sup>/K<sup>+</sup> pump.

498 The equations of the Na<sup>+</sup> in the three compartments are described by:

499 
$$d[Na^+]_o/dt = I_{Na}/(F \cdot vol_o) + 3 \cdot (i_{pump,N} + i_{pump,A}) - d_{Na_o} \cdot ([Na^+]_o - Na_{o_o})$$

500 
$$d[Na^+]_N/dt = -I_{Na}/(F \cdot vol_N) - 3 \cdot i_{pump,N} \cdot vol_o/vol_N - d_{Na_N} \cdot ([Na^+]_N - Na_{N_o})$$

501 
$$d[Na^+]_A/dt = -3 \cdot i_{pump,A} \cdot vol_o/vol_A - d_{Na_A} \cdot ([Na^+]_A - Na_{A_o})$$

502 See supplementary information for detailed formulas.

503

504 **Statistical analyses.** Required sample sizes were estimated based on our past experience  
505 performing similar experiments. Animals were randomly assigned to treatment groups.  
506 Analyses were performed in a manner blinded to treatment assignments in all behavioral  
507 experiments. Statistical analyses were performed using GraphPad Prism software v6. By pre-  
508 established criteria, values were excluded from the analyses if the viral injection or drug  
509 delivering sites were out of LHb. All statistical tests were two-tailed, and significance was  
510 assigned at  $P < 0.05$ . Normality and equal variances between group samples were assessed  
511 using the D'Agostino & Pearson omnibus normality test and Brown–Forsythe tests  
512 respectively. When normality and equal variance between sample groups was achieved, one-  
513 way ANOVAs (followed by Bonferroni's multiple comparisons test), or t test were used.  
514 Where normality or equal variance of samples failed, Mann-Whitney U test were performed.  
515 Linear regression test, Chi-square test was used inappropriate situations. The sample sizes,  
516 specific statistical tests used, and the main effects of our statistical analyses for each  
517 experiment are reported in Supplementary Table 1.

518 1 Henn, F. A. & Vollmayr, B. Stress models of depression: Forming genetically vulnerable strains.  
519 *Neurosci Biobehav R* **29**, 799-804, (2005).

520 2 Li, K. *et al.* beta CaMKII in Lateral Habenula Mediates Core Symptoms of Depression. *Science* **341**,  
521 1016-1020, (2013).

522 3 Powell, T. R., Fernandes, C. & Schalkwyk, L. C. in *Current Protocols in Mouse Biology* (John Wiley &  
523 Sons, Inc., 2011).

524

525

526

527

528 **References**

529  
530

- 531 1 Halassa, M. M. & Haydon, P. G. Integrated Brain Circuits: Astrocytic Networks  
532 Modulate Neuronal Activity and Behavior. *Annu Rev Physiol* **72**, 335-355, (2010).
- 533 2 Giaume, C., Koulakoff, A., Roux, L., Holcman, D. & Rouach, N. NEURON-GLIA  
534 INTERACTIONS Astroglial networks: a step further in neuroglial and gliovascular  
535 interactions. *Nat Rev Neurosci* **11**, 87-99, (2010).
- 536 3 Khakh, B. S. & Sofroniew, M. V. Diversity of astrocyte functions and phenotypes in  
537 neural circuits. *Nat Neurosci* **18**, 942-952, (2015).
- 538 4 Attwell, D. *et al.* Glial and neuronal control of brain blood flow. *Nature* **468**, 232-243,  
539 (2010).
- 540 5 Volterra, A. & Meldolesi, J. Astrocytes, from brain glue to communication elements:  
541 The revolution continues. *Nat Rev Neurosci* **6**, 626-640, (2005).
- 542 6 Woo, D. H. *et al.* TREK-1 and Best1 Channels Mediate Fast and Slow Glutamate  
543 Release in Astrocytes upon GPCR Activation. *Cell* **151**, 25-40, (2012).
- 544 7 Molofsky, A. V. *et al.* Astrocytes and disease: a neurodevelopmental perspective.  
545 *Gene Dev* **26**, 891-907, (2012).
- 546 8 Araque, A., Parpura, V., Sanzgiri, R. P. & Haydon, P. G. Tripartite synapses: glia, the  
547 unacknowledged partner. *Trends Neurosci* **22**, 208-215, (1999).
- 548 9 Harada, Y. *et al.* Expressional analysis of inwardly rectifying Kir4.1 channels in Noda  
549 epileptic rat (NER). *Brain Res* **1517**, 141-149, (2013).
- 550 10 Neusch, C. *et al.* Lack of the kir4.1 channel subunit abolishes K<sup>+</sup> buffering properties  
551 of Astrocytes in the ventral respiratory group: Impact on extracellular K<sup>+</sup> regulation  
552 (vol 95, pg 1843, 2006). *J Neurophysiol* **96**, 965-965, (2006).
- 553 11 Li, K. *et al.* beta CaMKII in Lateral Habenula Mediates Core Symptoms of Depression.  
554 *Science* **341**, 1016-1020, (2013).
- 555 12 Proulx, C. D., Hikosaka, O. & Malinow, R. Reward processing by the lateral habenula  
556 in normal and depressive behaviors. *Nat Neurosci* **17**, 1146-1152, (2014).
- 557 13 Li, B. *et al.* Synaptic potentiation onto habenula neurons in the learned helplessness  
558 model of depression. *Nature* **470**, 535-539, (2011).
- 559 14 Matsumoto, M. & Hikosaka, O. Lateral habenula as a source of negative reward  
560 signals in dopamine neurons. *Nature* **447**, 1111-U1111, (2007).
- 561 15 Shabel, S. J., Proulx, C. D., Trias, A., Murphy, R. T. & Malinow, R. Input to the Lateral  
562 Habenula from the Basal Ganglia Is Excitatory, Aversive, and Suppressed by  
563 Serotonin. *Neuron* **74**, 475-481, (2012).
- 564 16 Stamatakis, A. M. & Stuber, G. D. Activation of lateral habenula inputs to the ventral  
565 midbrain promotes behavioral avoidance. *Nat Neurosci* **15**, 1105-+, (2012).
- 566 17 Lammel, S. *et al.* Input-specific control of reward and aversion in the ventral  
567 tegmental area. *Nature* **491**, 212-+, (2012).
- 568 18 Sartorius, A. *et al.* Remission of Major Depression Under Deep Brain Stimulation of  
569 the Lateral Habenula in a Therapy-Refractory Patient. *Biol Psychiat* **67**, E9-E11,  
570 (2010).
- 571 19 Lecca, S. *et al.* Rescue of GABA(B) and GIRK function in the lateral habenula by  
572 protein phosphatase 2A inhibition ameliorates depression-like phenotypes in mice.  
573 *Nat Med* **22**, 254-261, (2016).



574 20 Shabel, S. J., Proulx, C. D., Piriz, J. & Malinow, R. GABA/glutamate co-release controls  
575 habenula output and is modified by antidepressant treatment. *Science* **345**, 1494-  
576 1498, (2014).

577 21 Cui, W. *et al.* Glial Dysfunction in the Mouse Habenula Causes Depressive-Like  
578 Behaviors and Sleep Disturbance. *Journal Of Neuroscience* **34**, 16273-16285, (2014).

579 22 Henn, F. A. & Vollmayr, B. Stress models of depression: Forming genetically  
580 vulnerable strains. *Neurosci Biobehav R* **29**, 799-804, (2005).

581 23 Adzic, M. *et al.* The contribution of hypothalamic neuroendocrine, neuroplastic and  
582 neuroinflammatory processes to lipopolysaccharide-induced depressive-like  
583 behaviour in female and male rats: Involvement of glucocorticoid receptor and  
584 C/EBP-beta. *Behavioural brain research* **291**, 130-139, (2015).

585 24 Olsen, M. L. & Sontheimer, H. Functional implications for Kir4.1 channels in glial  
586 biology: from K<sup>+</sup> buffering to cell differentiation. *J Neurochem* **107**, 589-601, (2008).

587 25 Djukic, B., Casper, K. B., Philpot, B. D., Chin, L. S. & McCarthy, K. D. Conditional  
588 knock-out of Kir4.1 leads to glial membrane depolarization, inhibition of potassium  
589 and glutamate uptake, and enhanced short-term synaptic potentiation. *The Journal  
590 of neuroscience : the official journal of the Society for Neuroscience* **27**, 11354-11365,  
591 (2007).

592 26 Tong, X. P. *et al.* Astrocyte Kir4.1 ion channel deficits contribute to neuronal  
593 dysfunction in Huntington's disease model mice. *Nat Neurosci* **17**, 694-703, (2014).

594 27 Kettenmann, H., Kettenmann, H. & Ransom, B. R. *Neuroglia*. 3rd edn, (Oxford  
595 University Press, 2013).

596 28 Ransom, C. B. & Sontheimer, H. Biophysical And Pharmacological Characterization Of  
597 Inwardly Rectifying K<sup>+</sup> Currents In Rat Spinal-Cord Astrocytes. *J Neurophysiol* **73**,  
598 333-346, (1995).

599 29 Newman, E. & Reichenbach, A. The Muller cell: A functional element of the retina.  
600 *Trends Neurosci* **19**, 307-312, (1996).

601 30 Amedee, T., Robert, A. & Coles, J. A. Potassium homeostasis and glial energy  
602 metabolism. *Glia* **21**, 46-55, (1997).

603 31 Neusch, C. *et al.* Lack of the Kir4.1 channel subunit abolishes K<sup>+</sup> buffering properties  
604 of astrocytes in the ventral respiratory group: impact on extracellular K<sup>+</sup> regulation. *J  
605 Neurophysiol* **95**, 1843-1852, (2006).

606 32 Newman, E. A. Inward-Rectifying Potassium Channels In Retinal Glial (Muller) Cells.  
607 *Journal Of Neuroscience* **13**, 3333-3345, (1993).

608 33 Rojas, L. & Orkand, R. K. K<sup>+</sup> channel density increases selectively in the endfoot of  
609 retinal glial cells during development of *Rana catesbiana*. *Glia* **25**, 199-203, (1999).

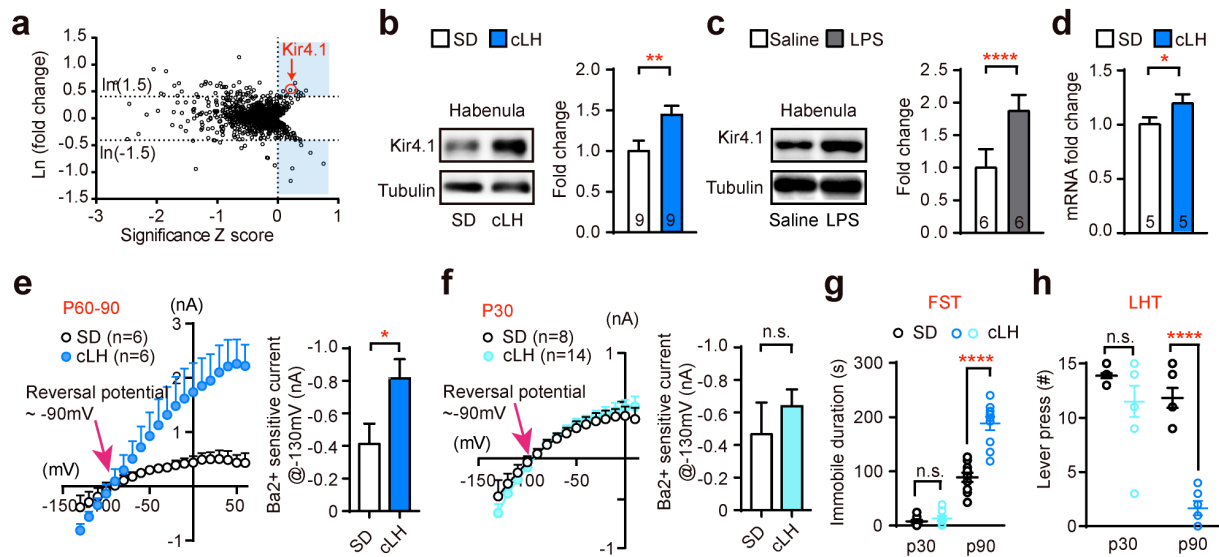
610 34 Li, L., Head, V. & Timpe, L. C. Identification of an inward rectifier potassium channel  
611 gene expressed in mouse cortical astrocytes. *Glia* **33**, 57-71, (2001).

612 35 Shigetomi, E. *et al.* Imaging calcium microdomains within entire astrocyte territories  
613 and endfeet with GCaMPs expressed using adeno-associated viruses. *J Gen Physiol*  
614 **141**, 633-647, (2013).

615 36 Hibino, H. *et al.* Inwardly Rectifying Potassium Channels: Their Structure, Function,  
616 and Physiological Roles. *Physiol Rev* **90**, 291-366, (2010).

617  
618  
619  
620

621  
622  
623



624  
625  
626  
627  
628  
629  
630  
631  
632  
633  
634  
635  
636  
637  
638  
639  
640  
641

**Figure 1 | Kir4.1 is upregulated in LHB of animal models of depression.**

**a**, Volcano plot of high-throughput proteomic screen identifies differentially expressed proteins in habenula of cLH rats. Ln (fold change) was Ln transformed value of the normalized protein ratio of cLH and control. Significance Z score was calculated as the average normalized ratio minus two folds of standard deviation. Proteins in the shaded areas have more than 50% significant change<sup>11</sup>. Kir4.1 is one of the eight upregulated proteins identified. Dash lines indicate fold change of 50%.

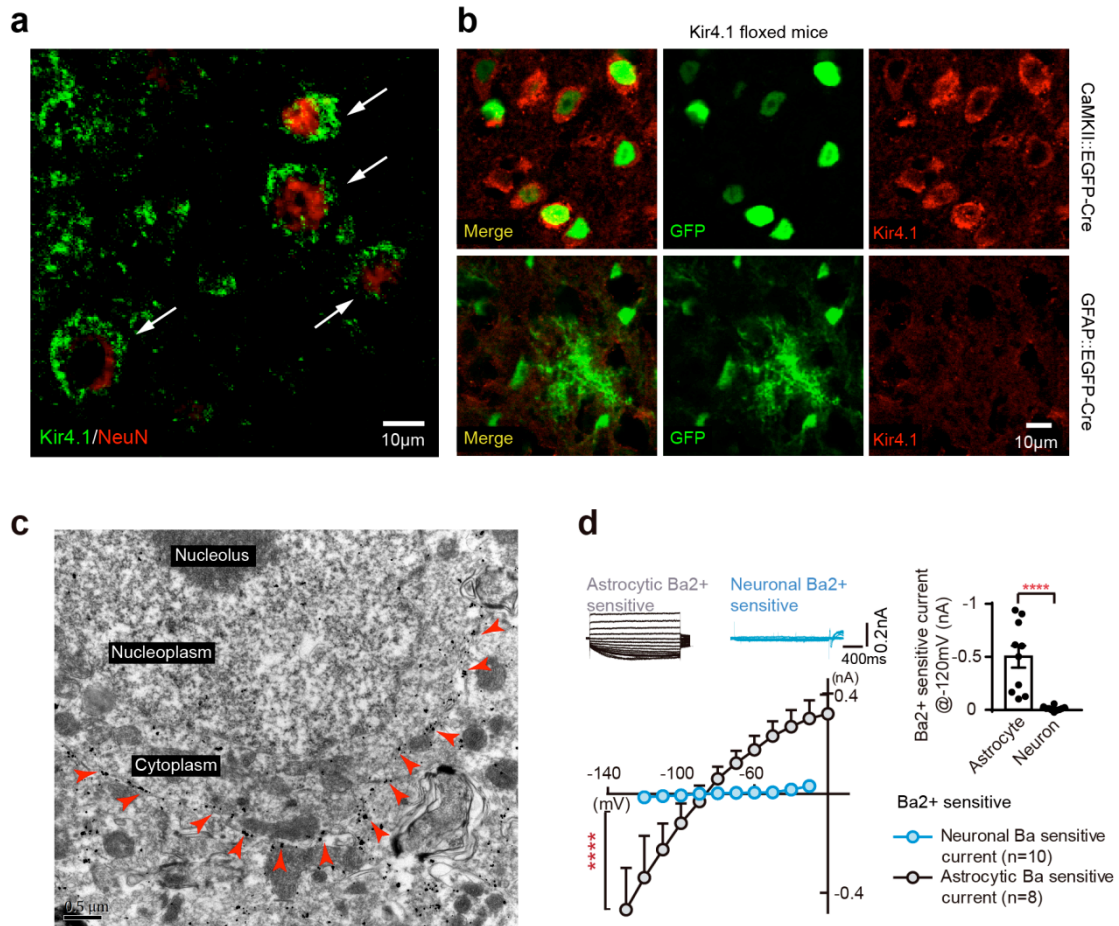
**b, c**, Western blot analysis showing upregulation of Kir4.1 protein in membrane fraction of habenula of cLH (**b**) and LPS-induced depression rat models (**c**). Tubulin is used as loading control. Numbers in the bars indicate the number of animals used.

**d**, QPCR analysis of Kir4.1 mRNA in habenula.

**e, f**, I-V plot and bar graph showing Ba<sup>2+</sup>-sensitive current in cLH rats and their wild type controls at the age of P60-90 (**e**) and P30 (**f**).

**g, h**, Age-dependent forced swim (FST, **g**) and learned helpless (LHT, **h**) phenotypes of cLH rats. Low number of lever press and high immobility time indicate depressive-like phenotype in P90 cLH rats.

Data are means ± SEM. \*P < 0.05, \*\*P < 0.01, \*\*\*\*P < 0.0001; n.s., not significant (See Supplementary Table 1 for statistical analysis and n numbers).



642  
643  
644  
645  
646  
647  
648  
649  
650  
651  
652  
653  
654  
655  
656  
657  
658  
659  
660  
661  
662

**Figure 2 | Kir4.1 is expressed on astrocytic processes tightly wrapping around neuronal soma in Lhb.**

a, Immunohistochemistry signals of Kir4.1 envelope neuronal soma as indicated by white arrows.  
b, The pan-soma Kir4.1 signals remain intact in Lhb of Kir4.1<sup>ff</sup> floxed mice injected with AAV2/1-CaMKII::EGFP-Cre, but are eliminated when injected with AAV2/5-GFAP::EGFP-Cre (GFAP: human astrocyte-specific GFAP promoter, *gfaABC1D*).  
c, Immunogold electron microscopy of Kir4.1. Red arrows indicate gold signals surrounding a neuronal soma.  
d, I-V plots of the Ba<sup>2+</sup> sensitive Kir4.1 current recorded in Lhb astrocytes and neurons, with representative traces shown in up-left and statistic bar graph of current recorded when cells are held at -120mV shown in up-right.

Data are means ± SEM. \*\*\*\*P < 0.0001 (See Supplementary Table 1 for statistical analysis and n numbers).

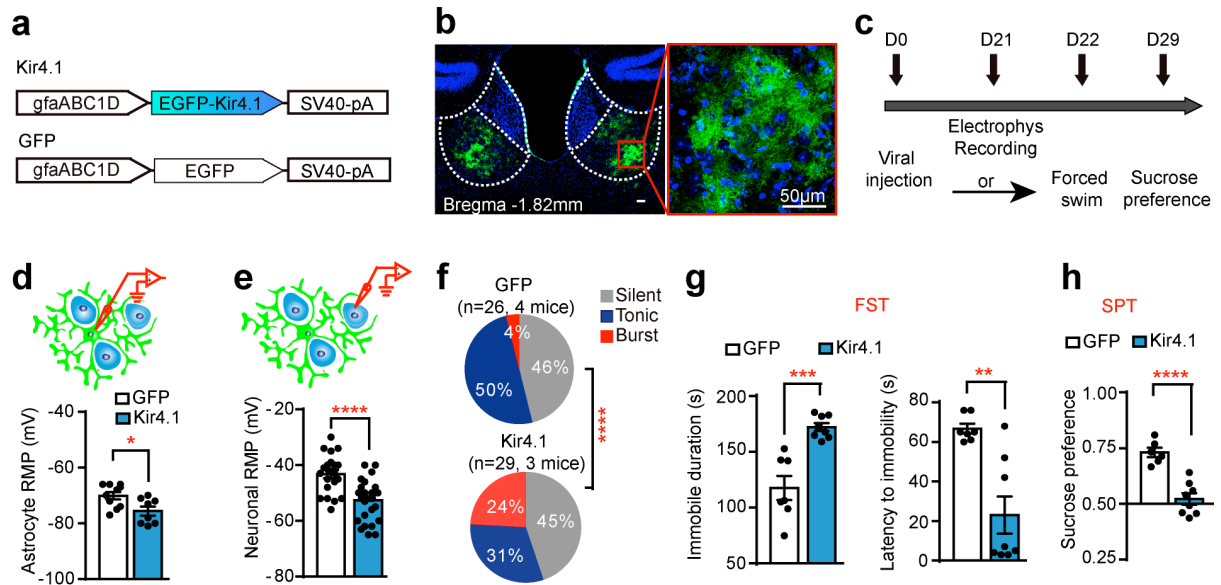


**Figure 3 | Astrocytic kir4.1 overexpression increases neuronal bursts in LHB and causes depressive-like phenotypes.**

**a**, Schematics of AAV vectors engineered to overexpress Kir4.1 or a GFP control and under a GFAP promoter.

**b**, Illustration of bilateral viral injection of AAV-GFAP::Kir4.1 in mouse LHB (stained with antibody against GFP and Hoechst).

**c**, Experimental paradigm for electrophysiology and behavioral testing.

**d-f**, Astrocytic overexpression of Kir4.1 decreases RMPs of both astrocytes (**d**) and neurons (**e**) and increases the bursting population in neurons (**f**).

**g, h**, Behavioral effects of expressing various viral constructs in LHB in forced swim test (FST) (**g**) and sucrose preference test (SPT) (**h**).

Data are means ± SEM. \*P < 0.05, \*\*P < 0.01, \*\*\*P < 0.001, \*\*\*\*P < 0.0001 (See Supplementary Table 1 for statistical analysis and n numbers).

663  
664  
665  
666  
667  
668  
669  
670  
671  
672  
673  
674  
675  
676  
677  
678  
679  
680  
681  
682  
683  
684  
685  
686  
687  
688  
689  
690

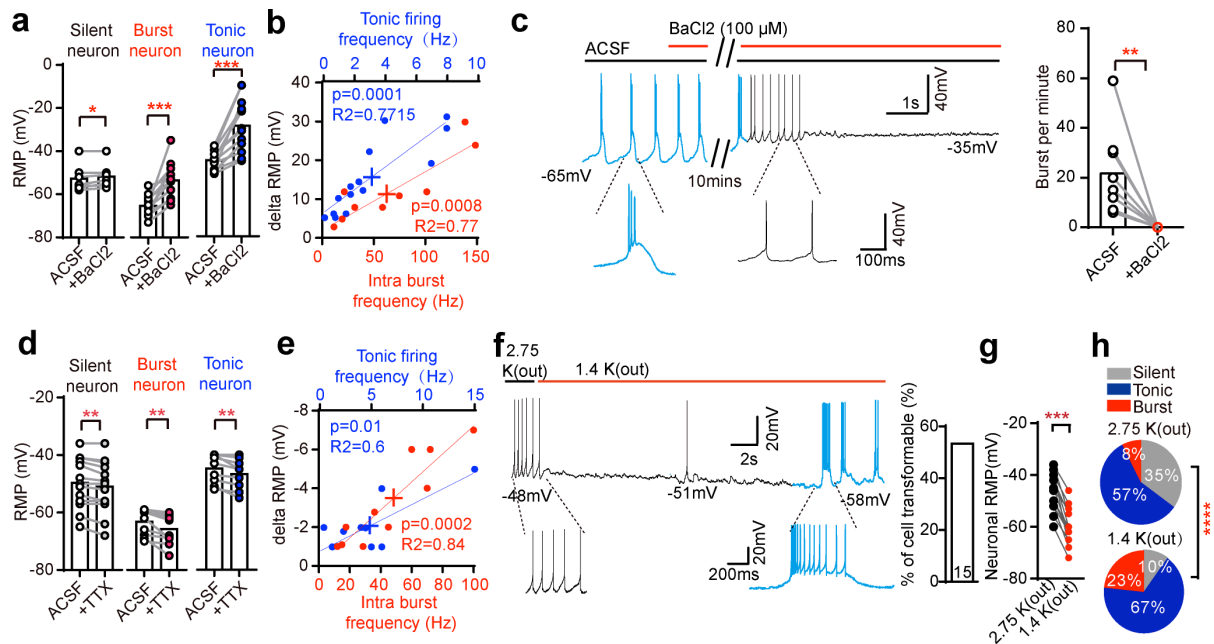


**Figure 4 | Kir4.1-dependent potassium buffering regulates neuronal RMP and bursting in Lhb.**  
**a, d**, Changes of neuronal RMPs caused by BaCl<sub>2</sub> (100 μM, **a**) or TTX (1 μM, **d**) in different neuronal types. RMPs are measured at 15min or 5min after perfusion of BaCl<sub>2</sub> or TTX, respectively, when the RMPs stabilize.  
**b, e**, Changes of neuronal RMPs after BaCl<sub>2</sub> (**b**) or TTX (**e**) treatments correlate with original firing rates of tonic-firing neurons (blue) or intra-burst frequencies of bursting neurons (red).  
**c**, Representative trace (left) and bar graph (right) showing BaCl<sub>2</sub> effect (sampled at 15mins after drug perfusion) onto bursting neurons. Spikes in bursting mode are marked in blue. Spikes in tonic-firing mode are marked in black.  
**f**, Example (left) and percentage of Lhb neurons transforming from tonic- to burst- firing mode after Kout is switched from normal (2.75 mM) to half (1.4mM) (sampled at 1min after drug perfusion).  
**g, h**, Lowering Kout to half decreases neuronal RMPs (**g**) and increases bursting neural population (**h**).

Data are means ± SEM. \*P < 0.05, \*\*P < 0.01, \*\*\*P < 0.001, \*\*\*\*P < 0.0001, n.s., not significant (See Supplementary Table 1 for statistical analysis and n numbers).

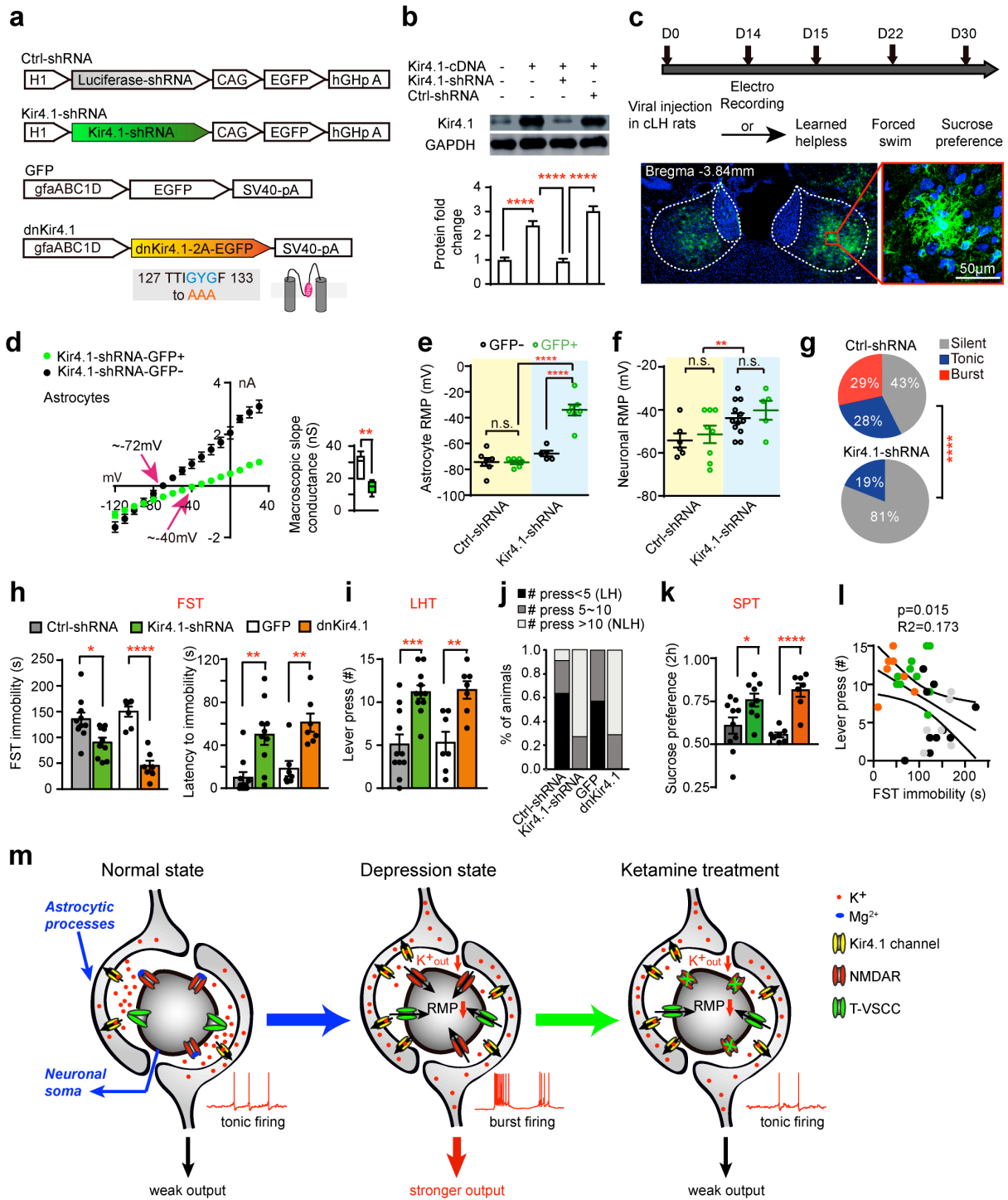


**Figure 5 | Loss of function of Kir4.1 in LHb decreases neuronal bursting and rescues depressive-like phenotypes of cLH rats.**

**a**, Schematics of the AAV vector engineered to overexpress shRNA or dominant negative form of Kir4.1. H1: human H1 promoter. CAG: The CMV early enhancer/chicken beta actin promoter. Three point mutations in the dnKir4.1 and their locations are indicated.

**b**, Western blot and quantification showing efficient knock-down of Kir4.1 by shRNA in HEK293T cells.

**c**, Experimental paradigm for behavioral testing of cLH rats infected by virus (top) and illustration of bilateral expression of AAV-GFAP::dnKir4.1 in LHb (stained with antibody against GFP and Hoechst).

**d-g**, AAV-Kir4.1-shRNA caused a shift of reverse potential from -72mV to -40mV in astrocytes (**d**), depolarization of astrocytes (**e**) and neurons in viral infected region (**f**), and abolished neuronal bursting (**g**).

Floating bars for membrane slope conductance in **d** is calculated from the I/V plots (between -120 and +40 mV).

**h-l**, AAV-Kir4.1-shRNA caused a shift of reverse potential from -72mV to -40mV in astrocytes (**d**), depolarization of astrocytes (**e**) and neurons in viral infected region (**f**), and abolished neuronal bursting (**g**).

Floating bars for membrane slope conductance in **d** is calculated from the I/V plots (between -120 and +40 mV).

708  
709

710

711

712

713

714

715

716

717

718

719

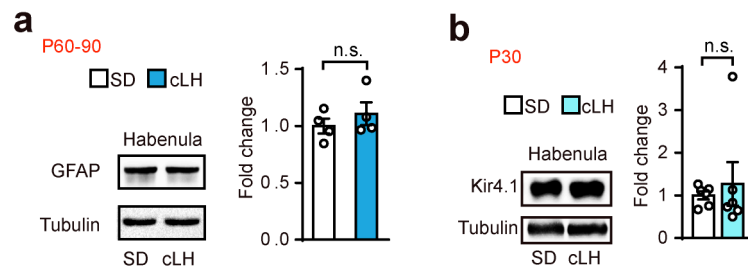
720

721

722 **h-k**, Behavioral effects of expressing various viral constructs in the LHb of cLH rats in FST (**h**), LHT (**i**,  
723 **j**) and SPT (**k**). **j**: Percentage of rats in each category. LH: learned helpless rats with <5 lever presses;  
724 NLH, non-learned helpless rats with >10 lever presses.  
725 **l**, FST immobility is highly correlated with learned helpless phenotype.  
726 **m**, A model for mechanisms of depression and ketamine treatment at LHb. Upregulation of Kir4.1 on  
727 astrocytic processes surrounding neuronal soma leads to enhanced K<sup>+</sup> buffering at the tight neuron-  
728 glia junction, decreased K<sub>out</sub> and hyperpolarized neuronal RMP. Consequently, de-inactivation of T-  
729 VSCCs initiates NMDAR-dependent bursts, causing a stronger output of LHb to trigger depression.  
730 Ketamine blockade of NMDARs stops bursts and relieves depression.  
731 Data are means ± SEM. \*P < 0.05, \*\*P < 0.01, \*\*\*P < 0.001, \*\*\*\*P < 0.0001, n.s., not significant (See  
732 Supplementary Table 1 for statistical analysis and n numbers).  
733  
734  
735  
736  
737  
738  
739  
740  
741  
742  
743  
744  
745  
746  
747  
748  
749  
750  
751  
752  
753  
754  
755  
756  
757  
758  
759  
760  
761  
762  
763  
764  
765

766 **Extended data**

767



768

769

770

771 **Extended Data Figure 1 | Kir4.1 is unchanged in p30 cLH rats.**

772 **a**, Western blot analysis showing no change of GFAP protein in habenula of cLH rats at the age of

773 P60-90.

774 **b**, Western blot analysis showing no change of Kir4.1 protein in membrane fraction of habenula in

775 cLH rats at the age of P30.

776 Data are means  $\pm$  SEM. n.s., not significant (See Supplementary Table 1 for statistical analysis and n

777 numbers).

778

779

780

781

782

783

784

785

786

787

788

789

790

791

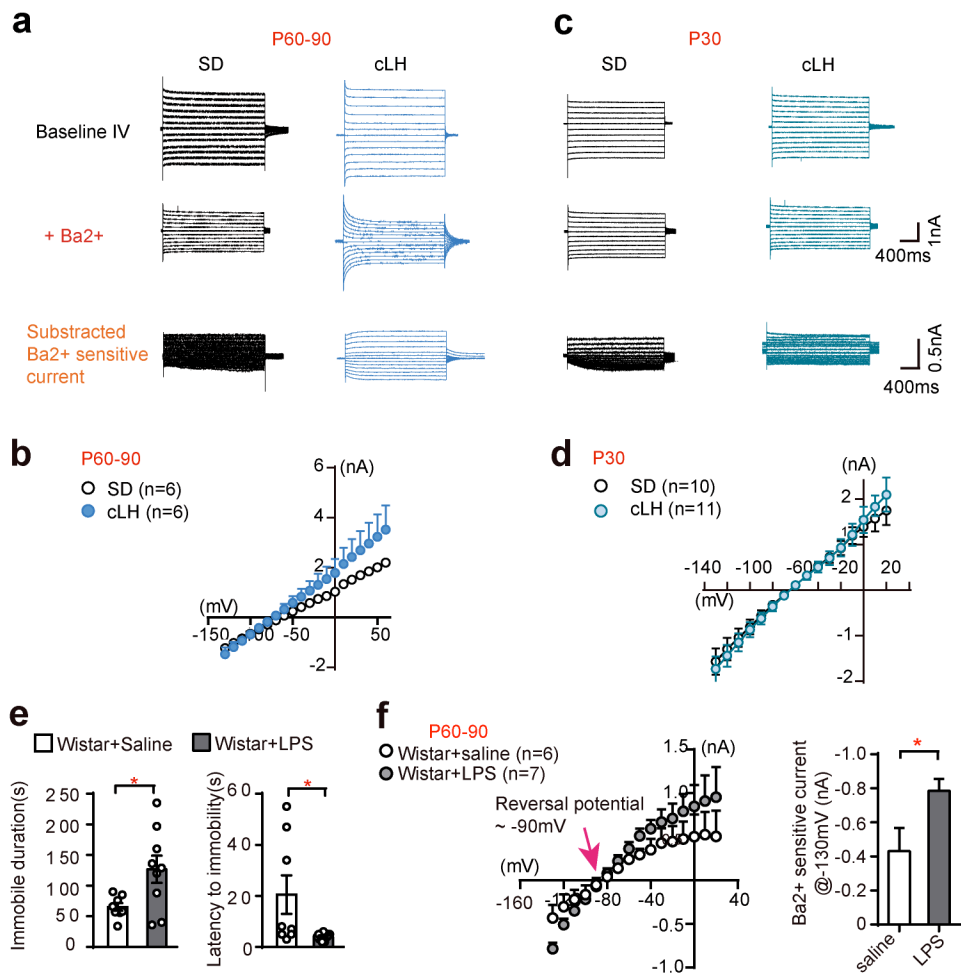
792

793

794

795





**Extended Data Figure 2 | Ba-sensitive Kir4.1 current is upregulated in LHB of adult cLH and LPS-induced depressive-like animals.**

**a, c,** Representative traces showing linear I-V curve in a typical astrocyte before (upper) and after (middle)  $Ba^{2+}$  perfusion under voltage linear steps (-130mV to -30 mV, step by 10mV, 2s duration, holding at -70mV). Subtraction of the two led to Ba-sensitive Kir current (bottom) in P60-90 (**a**) and P30 (**c**) cLH rats.

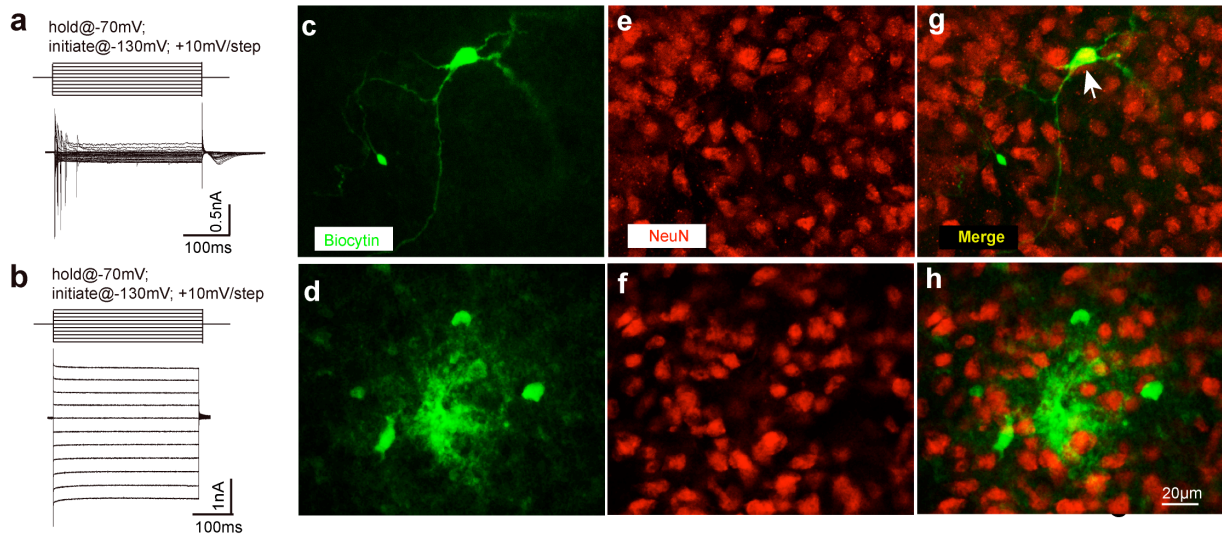
**b, d,** I-V plot of astrocytes in cLH rats and SD controls at the age of P60-90 (**b**) and P30 (**d**).

**e,** LPS injection (500  $\mu$ g/kg, i.p., for 7 days) induces increased immobile time and decreased latency to immobility in FST.

**f,** I-V plot and bar graph showing  $Ba^{2+}$ -sensitive current in LPS injected Wistar rats and their saline controls at the age of P60-90.

796  
797  
798  
799  
800  
801  
802  
803  
804  
805  
806  
807  
808  
809  
810

811



812

813

814

815

816

817

818

819

820

821

822

823

824

825

826

827

828

829

830

831

832

833

834

835

836

837

838

839

**Extended Data Figure 3 | Biocytin intercellular filling and double staining with NeuN confirm the identity of electrophysiologically identified neurons and astrocytes.**

**a, b**, A neuron (**a**) and an astrocyte (**b**) in LHB slices are first identified based on their specific morphology (astrocytes: 5-10μm diameter; neuron: ~15μm diameter) and physiological properties. The neuron fires at a depolarizing voltage step (**a**), whereas the astrocyte shows a steady-state I-V relationship and a lack of spiking activity (**b**). After electrophysiological characterization, cells are held for at least 30 minutes in voltage clamp and constantly injected with a hyperpolarization current (500ms, 50pA, 0.5Hz, 30min) to allow biocytin filling.

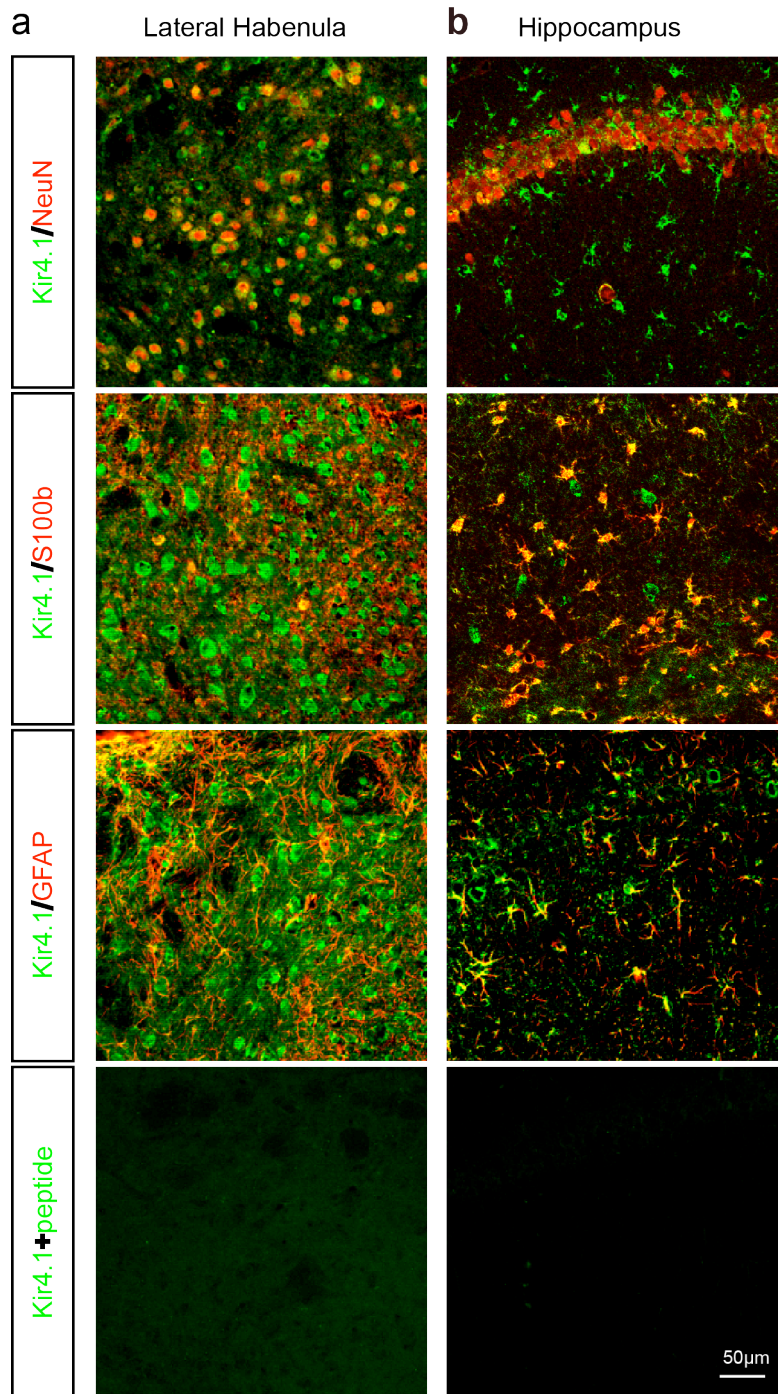
**c-h**, Biocytin labeled neurons and astrocytes subsequently confirmed by co-labeling with NeuN.

**c, d**, Biocytin signals in a single neuron (**c**) or a group of astrocytes due to diffusion through gap junctions (**d**).

**e, f**, NeuN signals.

**g, h**, Colabeling of NeuN with the neuron (indicated by white arrow, **g**) but not astrocytes (**h**).

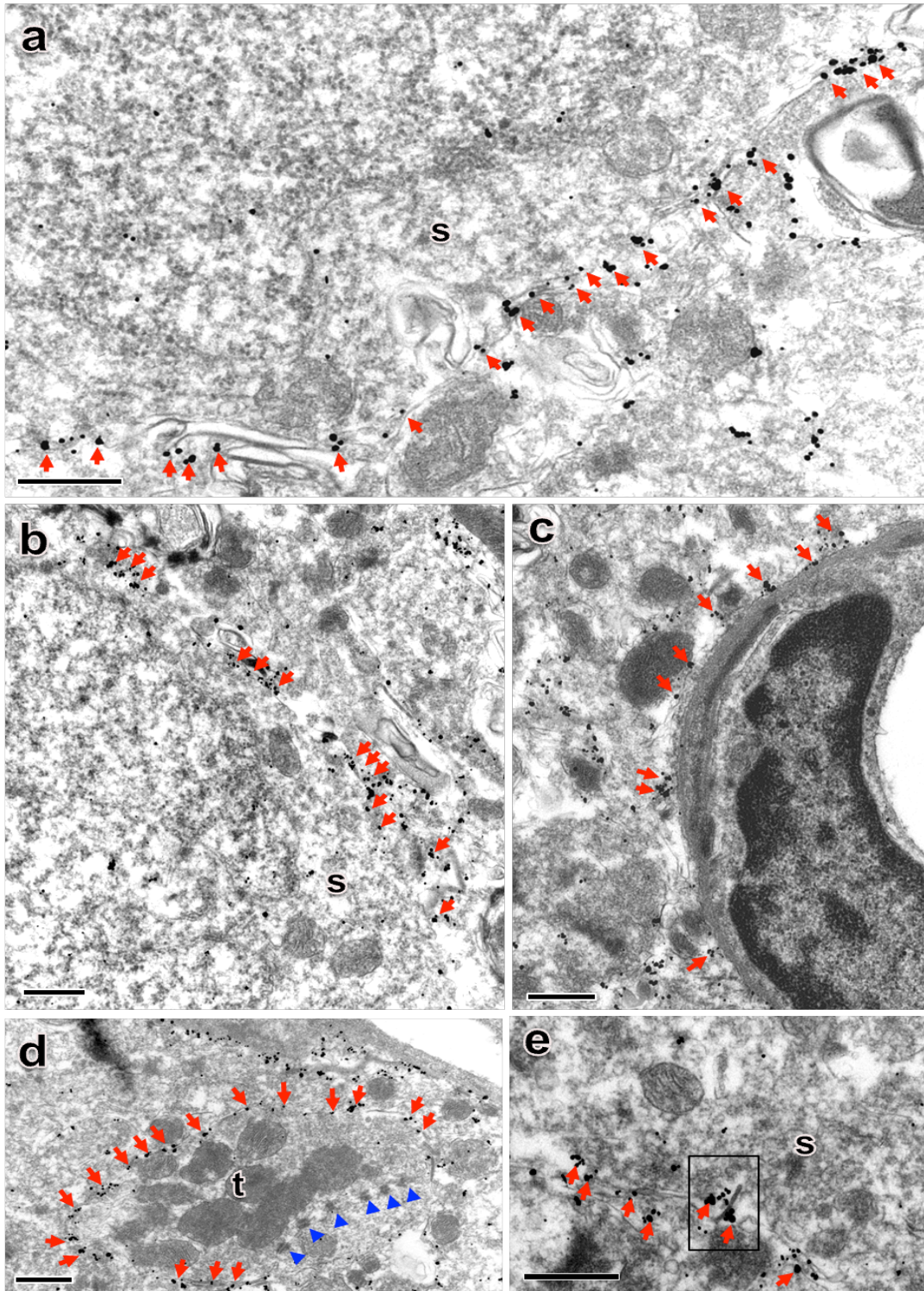
Note that all biocytin filled neurons (n = 18) show colabel with NeuN and all biocytin filled astrocytes (n = 11) do not colabel with NeuN.



840  
841  
842  
843  
844  
845  
846

**Extended Data Figure 4 | Expression pattern of Kir4.1 in Lhb and hippocampus.**

**a, b,** Kir4.1 co-immunostaining with neuronal marker (NeuN) or astrocytic marker (S100b and GFAP) in Lhb (**a**) or hippocampus (**b**). Bottom two panels are staining with the same kir4.1 antibody pre-incubated with the antigen peptide, demonstrating the specificity of Kir4.1 antibody.



847  
848  
849  
850  
851  
852  
853  
854  
855

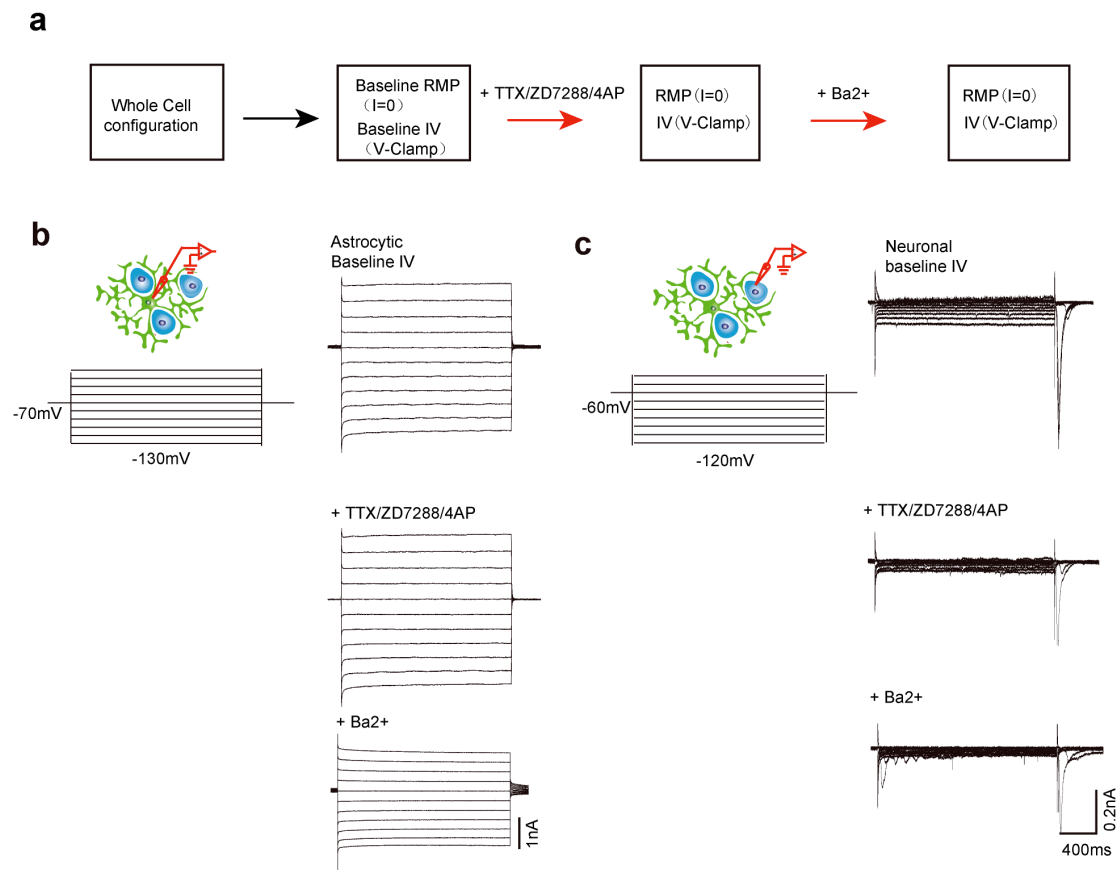
**Extended Data Figure 5 | Electron microscopy immunohistochemistry of Kir4.1 staining.**

**a-c,** Many Kir4.1 immunograin (arrows) surround the neuronal soma (**a**, **b**) and the vascular endothelial cell (**c**).

**d,** The Kir4.1 grains (arrows) also surround the axon-dendritic synapses, but are rare near the synaptic zones as indicated by the postsynaptic densities (arrowheads).

**e,** Insert shows Kir4.1 immunograin near a gap junction.

s: neuronal soma; t: axon terminal. Scale bars= 0.5 μm.



856  
857

858 **Extended Data Figure 6 | Kir4.1 is expressed in astrocytes but not neurons in LHb.**

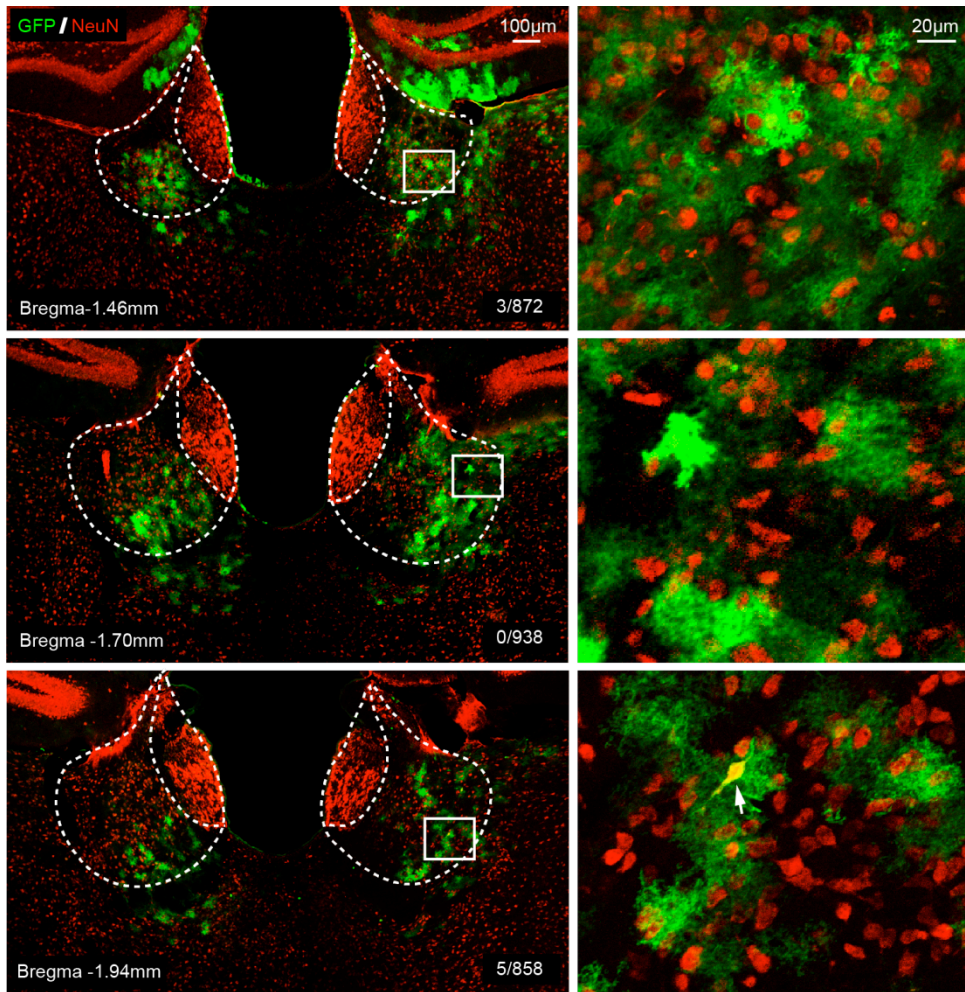
859 **a**, Schematics showing sequence of drug application and recording after a neuron or astrocyte is  
860 patched.

861 **b**, Representative traces showing a linear I-V curve in a typical astrocyte under voltage steps (-  
862 130mV to -30 mV, step by 10mV, 2s duration, holding at -70mV, protocol demonstrated on left) (upper  
863 panel). I-V curves of the same cell after addition of TTX (1uM), ZD7288 (50uM) and 4AP (1mM,  
864 middle), and further addition of Ba<sup>2+</sup> (100uM, bottom) are shown below.

865 **c**, Representative traces showing a non-linear I-V curve in a typical neuron under voltage steps (-  
866 130mV to -30 mV, step by 10mV, 2s duration, holding at -70mV, protocol demonstrated on left) (upper  
867 panel). I-V curves of the same cell after addition of TTX, ZD7288 and 4AP (middle), and further  
868 addition of Ba<sup>2+</sup> (bottom) are shown below.

869

870

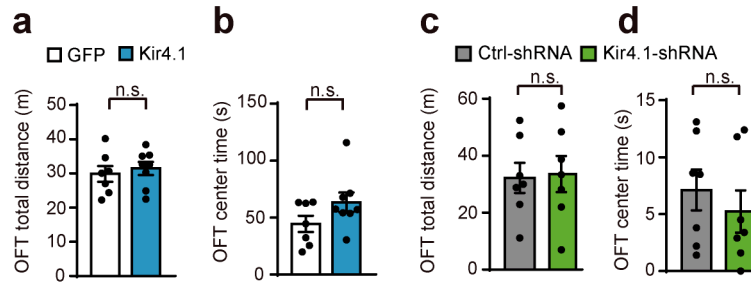


871  
 872  
 873  
 874  
 875  
 876  
 877  
 878  
 879  
 880  
 881  
 882  
 883  
 884  
 885  
 886  
 887  
 888  
 889  
 890  
 891  
 892  
 893

**Extended Data Figure 7 | Characterization of cell-type specificity of GFAP promoter driven expression of Kir4.1 in mouse LHB**

Double immunofluorescence for mouse NeuN (red) and GFP (green) in the coronal section of LHB brain slices infected with AAV-GFAP::Kir4.1 (AAV2/5-gfaABC1D-EGFP-Kir4.1) virus. Left are examples of anterior, middle and posterior coronal section of LHB. Numbers in the bottom right corner are the number of merged cells/ number of NeuN+ cells in the viral-infected area. Right are zoom-in images of the white square area in left. Note that there is only one infected neuron, as indicated by the white arrow, in all three fields of view.

894



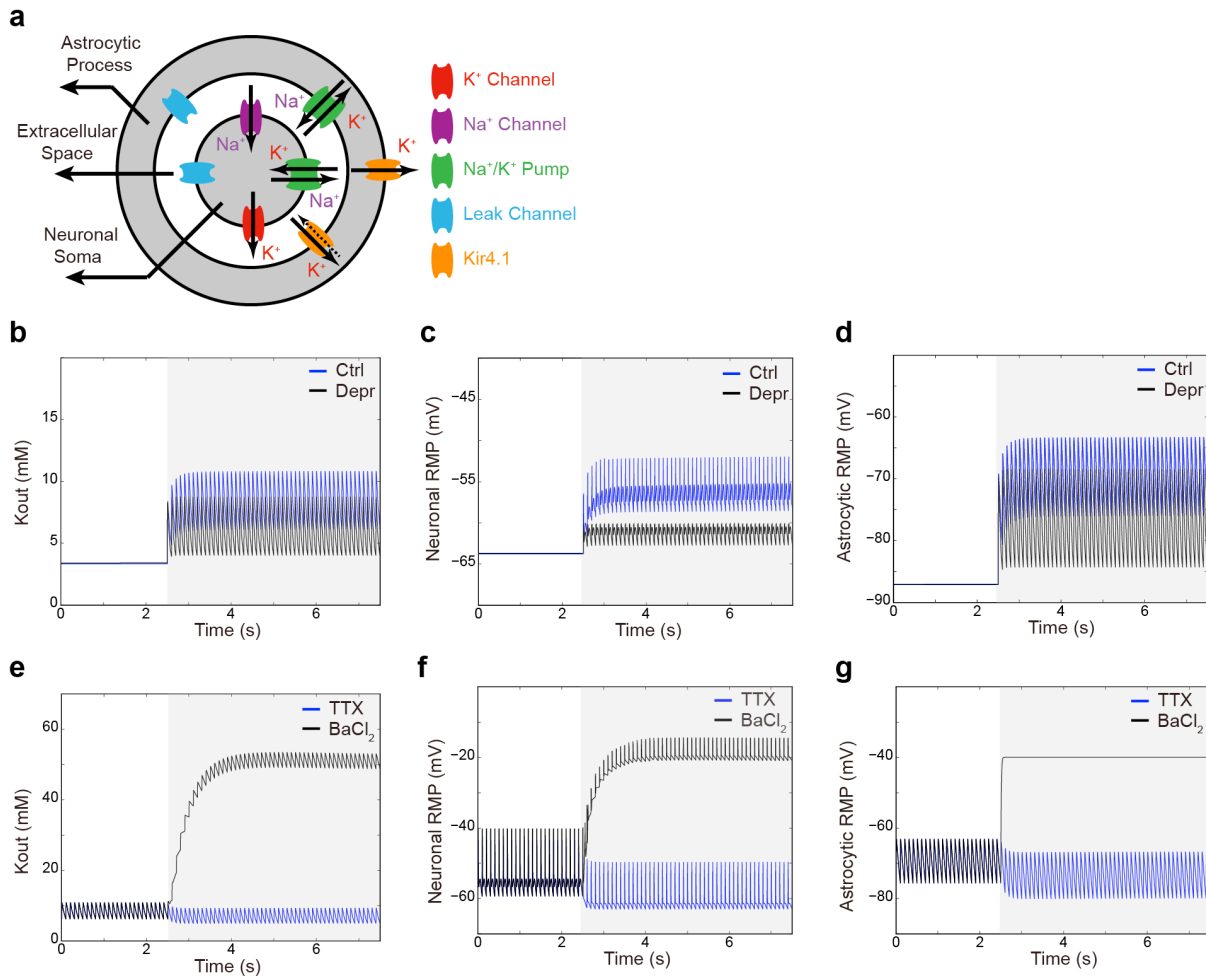
895  
896  
897  
898  
899  
900  
901  
902  
903  
904  
905

**Extended Data Figure 8 | Overexpression of Kir4.1 or Kir4.1-shRNA in LHb does not affect locomotion in open field test.**

**a-b,** Overexpression of Kir4.1 in LHb does not affect locomotion activities.

**c-d,** Overexpression of Kir4.1-shRNA in LHb does not affect locomotion activities.

Data are means  $\pm$  SEM. n.s., not significant (See Supplementary Table 1 for statistical analysis and n numbers).



907  
908  
909  
910  
911  
912  
913  
914  
915  
916  
917  
918  
919  
920  
921  
922  
923  
924  
925  
926  
927  
928  
929  
930  
931  
932  
933  
934

**Extended Data Figure 9 | Simulation of the dynamic potassium buffering effect of Kir4.1 in the tri-compartment model.**

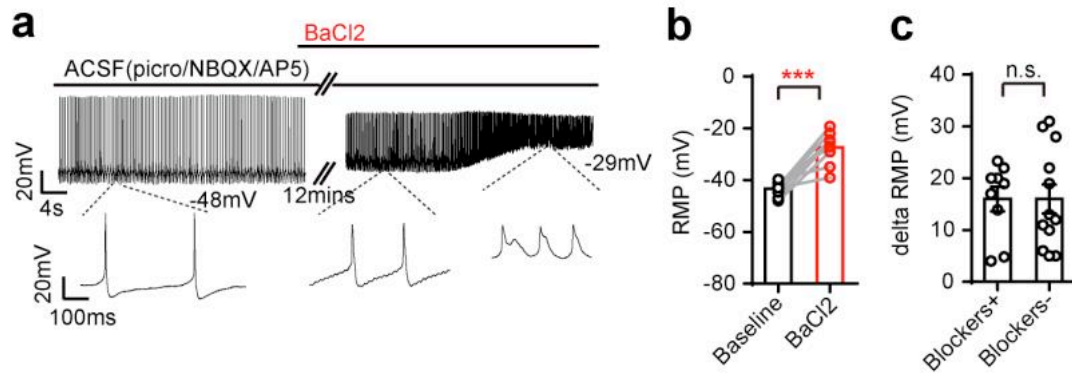
**a**, Schematic representation of a tri-compartment model involving neuron, astrocyte and extracellular space in between.

**b-d**, Effects of increasing Kir4.1 expression level on extracellular  $K^+$  concentration (**b**), neuronal membrane potential (**c**) and astrocytic membrane potential (**d**). Ctrl: control condition with 1x Kir4.1 conductance; Depr: depression condition with 2x Kir4.1 conductance. Grey shaded areas indicate application of 10 Hz tonic stimulation to neurons. Note that under this neuronal firing condition,  $K_{out}$  is lower, and neuron and astrocyte are more hyperpolarized in Depr than in Ctrl.

**e-g**, Effects of *in silico* TTX (blocking APs,  $g_{Na} = 0$ ) or  $Ba^{2+}$  (blocking Kir4.1,  $g_{Kir4.1} = 0$ ) treatments on extracellular  $K^+$  concentration (**e**), neuronal membrane potential (**f**) and astrocytic membrane potential (**g**) when neurons are under 10 Hz tonic stimulation. Grey shaded areas indicate *in silico* application of drugs. Note that TTX and  $Ba^{2+}$  cause opposite changes to  $K_{out}$ , neuronal membrane potential and astrocytic membrane potential.

Neuronal spikes are not shown for clarity of presentation.





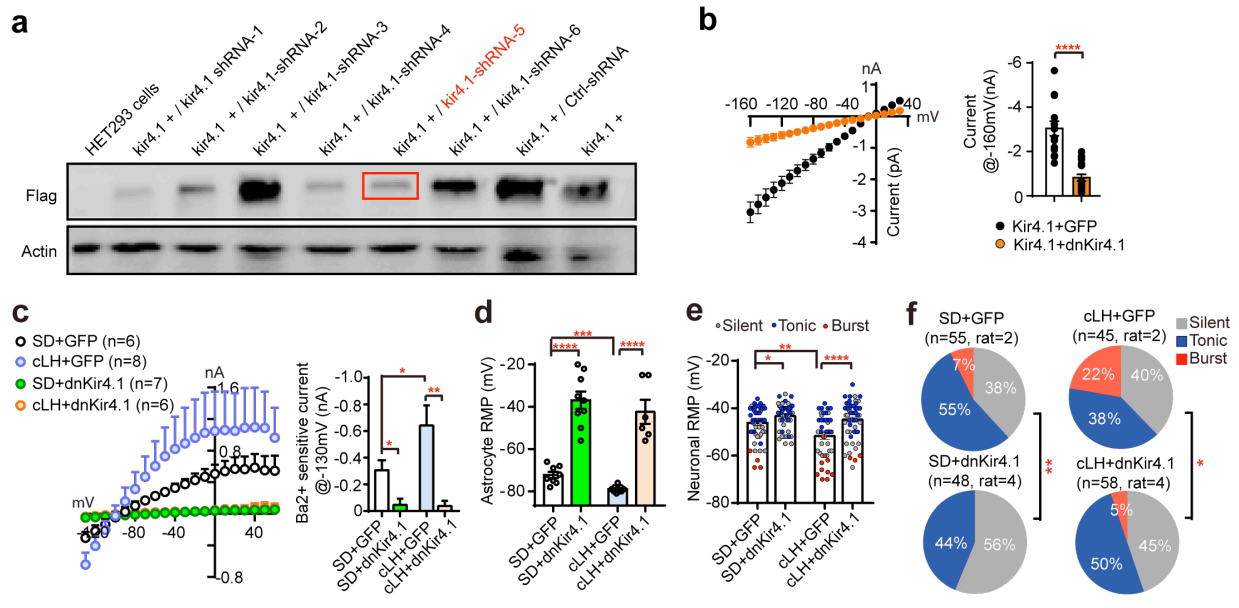
935  
936 **Extended Data Figure 10 | BaCl<sub>2</sub> caused depolarization of neuronal RMP in presence of**  
937 **synaptic transmitter blockers.**

938 a, b, Representative trace (a) and bar graph (b) showing effect of BaCl<sub>2</sub> (100uM) perfusion onto tonic-  
939 firing neurons which have been bathed with transmitter blockers (100 uM picrotoxin, 10 uM NBQX  
940 and 100 uM AP5).

941 c, Bar graph showing the level of RMP depolarization caused by BaCl<sub>2</sub> in presence or absence of  
942 transmitter blockers.

943 Data are means ± SEM. \*\*\*P < 0.001, n.s., not significant (See Supplementary Table 1 for statistical  
944 analysis and n numbers)

945  
946  
947  
948  
949  
950  
951  
952  
953  
954  
955  
956  
957  
958  
959  
960  
961  
962  
963  
964  
965  
966  
967  
968  
969  
970  
971  
972  
973  
974  
975  
976  
977  
978  
979  
980  
981  
982  
983



**Extended Data Figure 11 | Characterization of Kir4.1 loss-of-function constructs.**

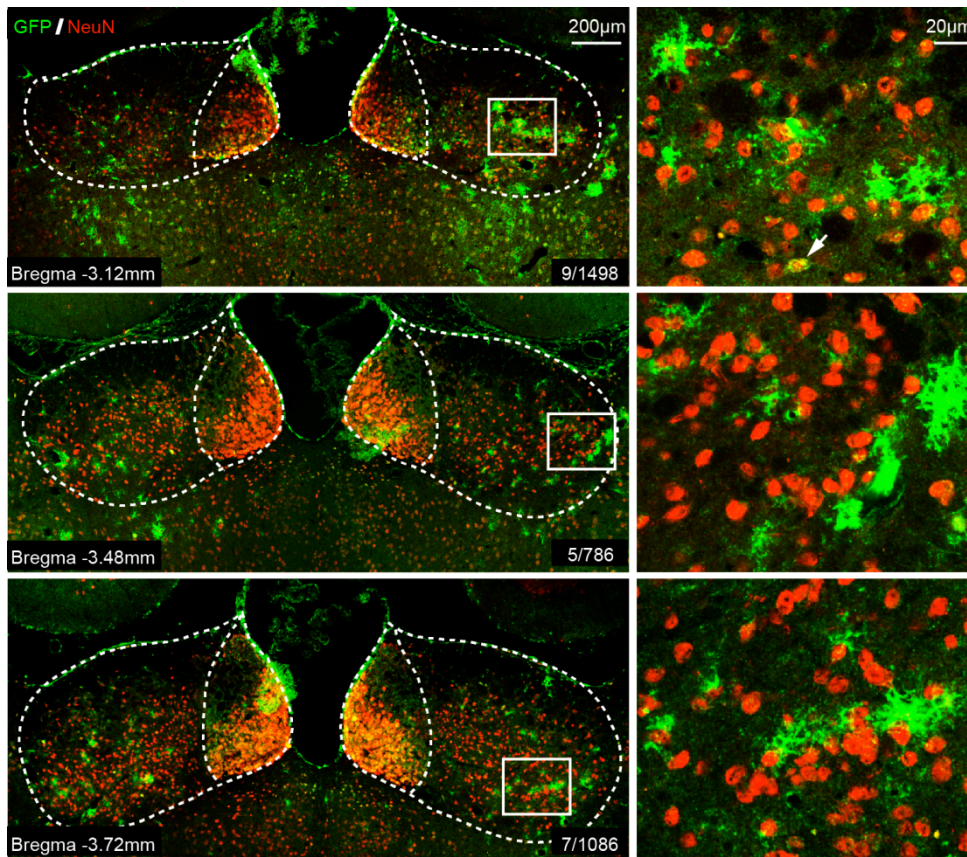
**a**, Flag-tagged-Kir4.1 plasmid (pAAV-CMV-betaGlobin-Kir4.1-eGFP-3Flag) was co-transfected with pAAV-vector expressing 6 different shRNAs (see Methods) of Kir4.1 or the negative control (shRNA of luciferase) into HEK293TN cell. Based on the knock-down efficiency as shown in the western blot, Kir4.1-shRNA-5 was chosen for viral package.

**b**, I-V plot showing Kir4.1 currents recorded in HEK293 cells transfected with pAAV-Kir4.1 together with negative control pAAV-GFP or pAAV-dnKir4.1 plasmid. Bars represent the current values recorded at -160mV.

**c**, I-V plot and bar graph showing Ba<sup>2+</sup>-sensitive currents blocked by AAV-dnKir4.1 in both cLH and SD rats.

**d-f**, AAV-dnKir4.1 caused a depolarization of RMP in astrocytes (d) and neurons in viral infected area (e), and abolished neuronal bursting (f) in both cLH and SD rats.

Data are means ± SEM. \*P < 0.05, \*\*P < 0.01, \*\*\*P < 0.001, \*\*\*\*P < 0.0001 (See Supplementary Table 1 for statistical analysis and n numbers).



1001  
 1002  
 1003  
 1004  
 1005  
 1006  
 1007  
 1008  
 1009  
 1010  
 1011  
 1012  
 1013  
 1014  
 1015  
 1016  
 1017  
 1018  
 1019  
 1020  
 1021  
 1022  
 1023  
 1024  
 1025  
 1026  
 1027  
 1028

**Extended Data Figure 12 | Characterization of cell-type specificity of GFAP promoter driven expression of dnKir4.1 in rat LHb.**

Double immunofluorescence for rat NeuN (red) and GFP (green) in the coronal section of LHb brain slices infected with AAV-GFAP::dnKir4.1 (AAV2/5-gfaABC1D-dnKir4.1-2A-eGFP) virus. Left are examples of anterior, middle and posterior coronal section of LHb. Numbers in the bottom right corner are the number of merged cells/ number of NeuN+ cells in the viral-infected area. Right are zoom-in images of the white square area in left. Note that there is only one infected neuron, as indicated by the white arrow, in all three fields of view.

# Contents

1

2 **Supplementary Table 1: Model parameters** .....

3 **Model description** .....

4

## 5 Supplementary Table 2: Model parameters

6

	Value	Unit	Parameter
R	8.31	$\text{J} \cdot \text{mol}^{-1} \cdot \text{K}^{-1}$	Gas constant
T	308	K	Absolute temperature
F	96485	$\text{C} \cdot \text{mol}^{-1}$	Faraday constant
<b>dt</b>	0.1	ms	Step time
<b>c<sub>N</sub></b>	30	pF	Neuronal capacitance
<b>c<sub>A</sub></b>	1	pF	Astrocytic capacitance
<b>g<sub>K</sub></b>	20	nS	Neuronal K <sup>+</sup> channel conductance
<b>g<sub>Na</sub></b>	120	nS	Neuronal Na <sup>+</sup> channel conductance
<b>g<sub>Leak,N</sub></b>	0.5	nS	Neuronal leak conductance
<b>V<sub>Leak,N</sub></b>	□50	mV	Neuronal leak potential
<b>i<sub>max,N</sub></b>	0.12	$\text{mM} \cdot \text{ms}^{-1}$	Neuronal Na <sup>+</sup> /K <sup>+</sup> pump rate
<b>g<sub>Kir</sub></b>	12	nS	Astrocytic Kir4.1 channel conductance on extracellular side
<b>g<sub>Kir_vess</sub></b>	12.5	nS	Astrocytic Kir4.1 channel conductance on vessel side
<b>g<sub>Leak,A</sub></b>	0.1	nS	Astrocytic leak conductance
<b>V<sub>Leak,A</sub></b>	□40	mV	Astrocytic leak potential
<b>i<sub>max,A</sub></b>	0.12	$\text{mM} \cdot \text{ms}^{-1}$	Astrocytic Na <sup>+</sup> /K <sup>+</sup> pump rate
<b>V<sub>h</sub></b>	178.46	mV	Kir4.1 channel parameter
<b>V<sub>s</sub></b>	119.47	mV	Kir4.1 channel parameter
<b>V<sub>rest,A</sub></b>	-10	mV	Kir4.1 channel parameter
<b>km<sub>K</sub></b>	3.0	mM	Na <sup>+</sup> /K <sup>+</sup> pump parameter
<b>km<sub>Na</sub></b>	10.	mM	Na <sup>+</sup> /K <sup>+</sup> pump parameter
<b>V<sub>N</sub></b>	□63.76	mV	Initial neuronal membrane potential
<b>V<sub>A</sub></b>	□87.08	mV	Initial astrocyte membrane potential
<b>[K<sup>+</sup>]<sub>N</sub></b>	135.04	mM	Initial neuronal K <sup>+</sup> concentration
<b>[K<sup>+</sup>]<sub>o</sub></b>	3.34	mM	Initial extracellular K <sup>+</sup> concentration
<b>[K<sup>+</sup>]<sub>A</sub></b>	135.00	mM	Initial astrocytic K <sup>+</sup> concentration
<b>[Na<sup>+</sup>]<sub>N</sub></b>	11.16	mM	Initial neuronal Na <sup>+</sup> concentration

$[\text{Na}^+]_o$	145.95	mM	Initial extracellular $\text{Na}^+$ concentration
$[\text{Na}^+]_A$	7.00	mM	Initial astrocytic $\text{Na}^+$ concentration
$\text{Vol}_o$	0.01	pL	Extracellular volume
$\text{Vol}_N$	1.08	pL	Neuronal volume
$\text{Vol}_A$	1.08	pL	Astrocytic volume
$d_{K_N}$	0.0001	$\text{ms}^{-1}$	$\text{K}^+$ effective flux rate in the neuron
$d_{K_o}$	0.001	$\text{ms}^{-1}$	$\text{K}^+$ effective flux rate in the extracellular space
$d_{K_A}$	0.1	$\text{ms}^{-1}$	$\text{K}^+$ effective flux rate in the astrocyte
$d_{\text{Na}_N}$	0.0001	$\text{ms}^{-1}$	$\text{Na}^+$ effective flux rate in the neuron
$d_{\text{Na}_o}$	0.01	$\text{ms}^{-1}$	$\text{Na}^+$ effective flux rate in the extracellular space
$d_{\text{Na}_A}$	0.01	$\text{ms}^{-1}$	$\text{Na}^+$ effective flux rate in the astrocyte
$[\text{K}^+]_{N_0}$	135	mM	Neuronal potassium concentration of the effective flux
$[\text{K}^+]_{o_0}$	3.5	mM	Extracellular potassium concentration of the effective flux
$[\text{K}^+]_{A_0}$	135	mM	Astrocytic potassium concentration of the effective flux
$[\text{Na}^+]_{N_0}$	12.0	mM	Neuronal sodium concentration of the effective flux
$[\text{Na}^+]_{o_0}$	144	mM	Extracellular sodium concentration of the effective flux
$[\text{Na}^+]_{A_0}$	7.0	mM	Astrocytic sodium concentration of the effective flux

---

7

## 8 **Model description**

9

10 The mathematical description of  $I_K$  and  $I_{Na}$  were achieved through a Hodgkin-Huxley style  
11 derivation of forward and backward rate equations<sup>1,2</sup>:

$$I_K = g_K \cdot n^4 \cdot (V_n - E_{Kn})$$

$$I_{Na} = g_{Na} \cdot m^3 \cdot h \cdot (V_n - E_{Nan})$$

12 where  $g_K$  and  $g_{Na}$  are the conductance of fast  $Na^+$  and  $K^+$  channel;  $E_{Kn}$  and  $E_{Nan}$  are the  
13 neuronal equilibrium potential for  $K^+$  and  $Na^+$ . The gate variables  $m$ ,  $h$ , and  $n$  are dimensionless  
14 activation and inactivation variables, which describe the activation and inactivation processes of  
15 the sodium and potassium channels, each of which is governed by the following differential  
16 equations:

$$dn/dt = \alpha_n(V_n) \cdot (1 - n) - \beta_n(V_n) \cdot n$$

$$dm/dt = \alpha_m(V_n) \cdot (1 - m) - \beta_m(V_n) \cdot m$$

$$dh/dt = \alpha_h(V_n) \cdot (1 - h) - \beta_h(V_n) \cdot h$$

17 where the forward and the backward rate  $\alpha$  and  $\beta$  describe the transition between the closed and  
18 open state of gate. The function of  $\alpha$  and  $\beta$  are given by:

$$\alpha_n(V_n) = 0.01 \cdot (V_n + 55) / (1 - \exp[(-V_n - 55)/10])$$

$$\beta_n(V_n) = 0.125 \cdot \exp[(-V_n - 65)/80]$$

$$\alpha_m(V_n) = 0.1 \cdot (V_n + 40) / (1 - \exp[(-V_n - 40)/10])$$

$$\beta_m(V_n) = 4 \cdot \exp[(-V_n - 65)/18]$$

$$\alpha_h(V_n) = 0.07 \cdot \exp[(-V_n - 65)/20]$$

$$\beta_h(V_n) = 1 / (\exp[(-V_n - 35)/10] + 1)$$

19 The neuronal membrane potential is highly dependent on the neuronal equilibrium potential for  $K^+$   
20 and  $Na^+$ , which are given by the Nernst equations:

$$E_{Kn} = R \cdot T / F \cdot \ln([K^+]_O / [K^+]_N)$$

$$E_{Nan} = R \cdot T / F \cdot \ln([Na^+]_O / [Na^+]_N)$$

21 where  $[K^+]_N$  and  $[K^+]_O$  are the neuronal and extracellular  $K^+$  concentration;  $[Na^+]_N$  and  
22  $[Na^+]_O$  are the neuronal and extracellular  $Na^+$  concentration;  $R$ ,  $T$  and  $F$  are the gas constant,  
23 absolute temperature and faraday constant.

24 Neuronal leak current is described by:

$$I_{\text{Leak,N}} = g_{\text{Leak,N}} \cdot (V_n - E_{\text{Leak,N}})$$

25 where  $g_{\text{Leak,N}}$  is the neuronal leak conductance and  $E_{\text{Leak,N}}$  is the neuronal leak potential.

26 The formula of Kir4.1 channel was modified from a previous model<sup>3</sup>:

$$I_{\text{Kir}} = g_{\text{Kir}} \cdot \sqrt{[\text{K}^+]_o} / (1 + \exp((V_A + V_{\text{restA}} - E_{\text{Ka}} + V_h) / V_s)) (V_A + V_{\text{restA}} - E_{\text{Ka}})$$

$$I_{\text{Kir,vess}} = g_{\text{Kir,vess}} \cdot \sqrt{[\text{K}^+]_{\text{O},0}} / (1 + \exp((V_A + V_{\text{restA}} - E_{\text{Ka,vess}} + V_h) / V_s)) (V_A + V_{\text{restA}} - E_{\text{Ka,vess}})$$

27 where  $g_{\text{Kir}}$  and  $g_{\text{Kir,vess}}$  are the conductance of Kir4.1 channel on the extracellular and vessel

28 side respectively.

29 Astrocytic equilibrium potential for  $\text{K}^+$  and  $\text{Na}^+$  are given by:

$$E_{\text{Ka}} = R \cdot T / F \cdot \ln([\text{K}^+]_o / [\text{K}^+]_A)$$

$$E_{\text{Naa}} = R \cdot T / F \cdot \ln([\text{Na}^+]_o / [\text{Na}^+]_A)$$

30 where  $[\text{K}^+]_A$  and  $[\text{Na}^+]_A$  are the astrocytic  $\text{K}^+$  and  $\text{Na}^+$  concentration.

31 The astrocyte membrane potential equation also comprises a leak term:

$$I_{\text{Leak,A}} = g_{\text{Leak,A}} \cdot (V_A - E_{\text{Leak,A}})$$

32 The equation of the  $\text{Na}^+/\text{K}^+$  pump depends on the extracellular  $\text{K}^+$  and intracellular  $\text{Na}^+$

33 concentrations as:

$$i_{\text{pump,N}} = i_{\text{max,N}} \cdot (1 + km_{\text{K}} / [\text{K}^+]_o)^{-2} \cdot (1 + km_{\text{Na}} / [\text{Na}^+]_N)^{-3}$$

$$i_{\text{pump,A}} = i_{\text{max,A}} \cdot (1 + km_{\text{K}} / [\text{K}^+]_o)^{-2} \cdot (1 + km_{\text{Na}} / [\text{Na}^+]_A)^{-3}$$

34 where  $i_{\text{max,N}}$  and  $i_{\text{max,A}}$  are the  $\text{Na}^+/\text{K}^+$  pump rate for neuron and astrocyte respectively.

35 The kinetics of ion concentrations are calculated as:

$$d[\text{K}^+]_o / dt = (I_{\text{Kir}} + I_{\text{K}}) / (F \cdot \text{Vol}_o) - 2i_{\text{pump,A}} - 2i_{\text{pump,N}} - d_{\text{K},o} \cdot ([\text{K}^+]_o - [\text{K}^+]_{\text{O},0})$$

$$d[\text{K}^+]_N / dt = -I_{\text{K}} / (F \cdot \text{Vol}_N) + 2i_{\text{pump,N}} \cdot \text{Vol}_o / \text{Vol}_N - d_{\text{K},N} \cdot ([\text{K}^+]_N - [\text{K}^+]_{\text{N},0})$$

$$d[\text{K}^+]_A / dt = (-I_{\text{Kir}} - I_{\text{Kir,vess}}) / (F \cdot \text{Vol}_A) + 2i_{\text{pump,A}} \cdot \text{Vol}_o / \text{Vol}_A - d_{\text{K},A} \cdot ([\text{K}^+]_A - [\text{K}^+]_{\text{A},0})$$

$$d[\text{Na}^+]_o / dt = I_{\text{Na}} / (F \cdot \text{Vol}_o) + 3i_{\text{pump,A}} + 3i_{\text{pump,N}} - d_{\text{Na},o} \cdot ([\text{Na}^+]_o - [\text{Na}^+]_{\text{O},0})$$

$$d[\text{Na}^+]_N / dt = -I_{\text{Na}} / (F \cdot \text{Vol}_N) - 3i_{\text{pump,N}} \cdot \text{Vol}_o / \text{Vol}_N - d_{\text{Na},N} \cdot ([\text{Na}^+]_N - [\text{Na}^+]_{\text{N},0})$$

$$d[\text{Na}^+]_A / dt = -3i_{\text{pump,A}} \cdot \text{Vol}_o / \text{Vol}_A - d_{\text{Na},A} \cdot ([\text{Na}^+]_A - [\text{Na}^+]_{\text{A},0})$$

36 where  $\text{Vol}_o$ ,  $\text{Vol}_N$  and  $\text{Vol}_A$  are the volumes of the extracellular, neuronal and astrocytic

37 compartments. The term  $d \cdot ([X] - [X_0])$  accounts for the diffusion effect, where  $d$  is the rate of this

38 effective flux,  $[X]$  is the ionic concentration and  $[X_0]$  is the equilibrium concentration.



39 Simulations were solved numerically with an explicit Runge-Kutta Prince-Dormand 8th-9th order  
40 method with the GSL library in cython and python. The parameters used in the model are  
41 presented in Supplementary Table 1.

42

### 43 **References**

- 44 1 Abbott, L. F. & Kepler, T. B. in *Statistical Mechanics of Neural Networks: Proceedings of*  
45 *the XIth Sitges Conference Sitges, Barcelona, Spain, 3–7 June 1990* (ed Luis Garrido)  
46 5-18 (Springer Berlin Heidelberg, 1990).
- 47 2 Gerstner, W. & Kistler, W. M. *Spiking neuron models : single neurons, populations,*  
48 *plasticity.* (Cambridge University Press, 2002).
- 49 3 Sibille, J., Dao Duc, K., Holcman, D. & Rouach, N. The neuroglial potassium cycle  
50 during neurotransmission: role of Kir4.1 channels. *PLoS computational biology* **11**,  
51 e1004137 (2015).

52